Chapter 3.6

Hyperspectral imaging in medical applications

Baowei Fei[a,b,c,*]

[a]*Department of Bioengineering, The University of Texas at Dallas, Richardson, TX, United States;* [b]*Department of Radiology, The University of Texas Southwestern Medical Center, Dallas, TX, United States;* [c]*Advanced Imaging Research Center, The University of Texas Southwestern Medical Center, Dallas, TX, United States*

**Corresponding author.*

1. Introduction

Hyperspectral imaging (HSI) also called imaging spectrometer [1] was originated from remote sensing and has been explored for various applications by NASA [2]. With the advantages of acquiring two-dimensional images across a wide range of electromagnetic spectrum, HSI has been applied to numerous areas including archaeology and art conservation [3,4], vegetation and water resource control [5,6], food quality and safety control [7,8], forensic medicine [9,10], crime scene detection [11,12], and biomedical area [13,14].

As an emerging imaging modality for medical applications, HSI offers great potential for noninvasive disease diagnosis and surgical guidance. Light delivered to the biological tissues undergoes multiple scattering from inhomogeneity of biological structures and absorption primarily in hemoglobin, melanin, and water as it propagates through tissue [15,16]. It is assumed that the absorption, fluorescence, and scattering characteristics of tissue change during the progression of disease [17], therefore the reflected, fluorescent and transmitted light from tissue captured by HSI carries quantitative diagnostic information about tissue pathology [17–20]. In recent years, the advancements of hyperspectral cameras, image analysis methods, and computational power make it possible for many exciting applications in the medical field.

In the following, we aim to introduce and explain medical hyperspectral imaging (MHSI) technology and to give an overview of the literature on MHSI hardware, software, and applications. This chapter covers the literature until spring 2013. We start at the basics, with the mechanisms of HSI and its current

Hyperspectral Imaging. https://doi.org/10.1016/B978-0-444-63977-6.00021-3

development status. We then classify MHSI based on its acquisition mode, spectral range and spatial resolution, measurement mode, dispersive devices, detector arrays, and combination with other techniques. Image analysis methods for MHSI are summarized with an emphasis on preprocessing, feature extraction and selection, and classification methods. The part on applications is a reference of the literature available on disease diagnosis and surgery guidance. Finally, we conclude with a discussion on the achievements of the past years and some future challenges.

2. Tissue optics

The propagation of light within a tissue is an important problem in medical applications and development of diagnostic methods. Therefore, this section is dedicated to a brief review of the light tissue interaction mechanisms, optical processes involved in HSI, and useful diagnostic information provided by HSI.

Biological tissues are heterogeneous in composition with spatial variations in optical properties [21]. Light entering biological tissues undergoes multiple scattering and absorption events as it propagates across the tissue [22]. Scattering occurs where there is a spatial variation in the refractive index [21]. In cellular media, the important scatters are the subcellular organelles, with their size running from <100 nm to 6 μm. For example, mitochondria are the dominant scatterers among the organelles. The structure of a lipid membrane and lipid folds running inside gives mitochondria a high optical contrast to the surrounding cytoplasm and produces the observed strong scattering effects. The shape and size of the cells vary among different tissue types with dimensions of a few microns and larger. Although an isolated cell can be a strong scatterer, within a tissue the scattering is largely subcellular in origin [21]. The scattering properties of support tissues composed of cells and extracellular proteins (elastin and collagen, etc.) are caused by the small-scale inhomogeneities and the large-scale variations in structures they form.

The penetration ability of light into biological tissues depends on how strongly the tissue absorbs light. Most tissues are sufficiently weak absorbers to permit significant light penetration within the therapeutic window, ranging from 600 to 1300 nm [21]. Within the therapeutic window, scattering is over absorption, so the propagating light becomes diffuse. Tissue absorption is a function of molecular composition. Molecules absorb photons when the photon's energy matches an interval between internal energy states, and the transition between quantum states obeys the selection rules for the species. During absorption processing, transitions between two energy levels of a molecule that are well defined at specific wavelengths could serve as a spectral fingerprint of the molecule for diagnostic purposes [21,23]. For example, absorption spectra characterize the concentration and oxygen saturation of hemoglobin, which reveals two hallmarks of cancer: angiogenesis and hypermetabolism [16]. Tissue components absorbing light are called

chromophores. Some of the most important chromophores for visible (vis) wavelengths are blood and melanin, of which the absorption coefficient decreases monotonically with increasing wavelength. The primary absorbers for UV wavelengths are protein and amino acids, while the important absorbing chromophore for IR wavelengths is water [24].

The light absorbed by tissue constituents (reduced nicotinamide adenine dinucleotide (NADH), hemoglobin, melanin, water, etc.) is either converted to heat or radiated in the form of luminescence including fluorescence and phosphorescence [18,21,25]. Fluorescence that originates from endogenous fluorescent chromophores is also called autofluorescence. Incident light typically in the ultraviolet or visible region excites the tissue molecules and induces fluorescence emission. The majority of the endogenous fluorophores are associated with the structural matrix of tissue or with various cellular metabolic pathways [21,26]. The most common fluorophores in the structural matrix are collagen and elastin, while the predominant fluorophores involved in cellular metabolism are the NADH, flavin adenine dinucleotide, and lipopigments [27]. These intrinsic fluorophores exhibit different strengths and covers various spectral ranges in the ultraviolet and visible regions. For example, fluorescence from collagen or elastin using excitation between 300 and 400 nm shows broad emission bands between 400 and 600 nm, which can be used to distinguish various types of tissues, e.g., epithelial and connective tissues [28]. Cells in different disease states often have different structures, or undergo different rate of metabolism, which result in different fluorescence emission spectra. Therefore, fluorescence imaging makes it possible to investigate tissues for diagnosis of diseases in real time without administrating exogenous fluorescent agents [21]. Various exogenous fluorophores have also been created and studied for biological diagnostics using HSI [27], but this chapter will mainly discuss the intrinsic fluorescence.

Incident light can be directly reflected on the surface of the tissue, or be scattered due to random spatial variations in tissue density (membranes, nuclei, etc.) and then be remitted to the tissue surface [25]. Light becomes randomized in direction due to multiple scattering, and this is known as diffuse reflectance, which provides information about scattering and absorbing components deep within the tissue [29]. The measured reflectance signal represents light that has sampled a variety of sampling depths within the tissue and is therefore an average measure of the properties over a certain volume of tissue [29]. Significant scatterers present in tissue include collagen, keratin, nuclei, and mitochondria; however, other smaller subcellular components (e.g., lysosomes, membranes) also scatter light. Knowledge of the origin of the scattering and absorption signal would facilitate accurate modeling and interpretation of the reflectance data. The reflectance signal measured from epithelial tissue is determined by the structural and biochemical properties of the tissue; therefore, analyzing changes in optical properties can be used to noninvasively probe the tissue microenvironment [29]. Alterations in tissue

morphology, including hyperplasia, nuclear crowding, degradation of collagen in the extracellular matrix by matrix metalloproteinases, and increased nuclear/cytoplasmic ratio, which are associated with disease progression, can affect the scattering signal. As diseases progress, hemoglobin absorption may be affected by angiogenesis, tissue hypoxia, etc. Therefore, changes in the disease states should lead to corresponding changes in the patterns of the light reflected from the tissue.

Reflectance imaging can detect local changes in scattering and absorption of tissue, and fluorescence imaging can probe changes in the biochemical composition of tissue by revealing levels of endogenous fluorophores [30]. Multimodal HSI combining reflectance and fluorescence has been investigated for cancer diagnosis [19,31]. Furthermore, HSI system can be adapted to other existing techniques, such as microscope, and colposcope, to provide complementary information in a more accurate and reliable manner. Transmission HSI microscope is one example of these combinatory technologies and has been used in tissue pathology.

3. Hardware and systems

HSI generates a three-dimensional (3D) data set of spatial and spectral information known as hypercube (shown in Fig. 1). With spatial information, the source of each spectrum on samples can be located, which makes it possible to probe more completely the light interactions with pathology. The spectral signature of each pixel in the images enables HSI to identify various pathological conditions. HSI generally covers a contiguous portion of the light spectrum with more spectral bands (up to a few hundreds) and higher spectral resolution than multispectral imaging (such as RGB color cameras), therefore, HSI is able to capture the subtle spectral differences under different pathological conditions while multispectral imaging may miss significant spectral information for diagnostics. Moreover, HSI spectrograph

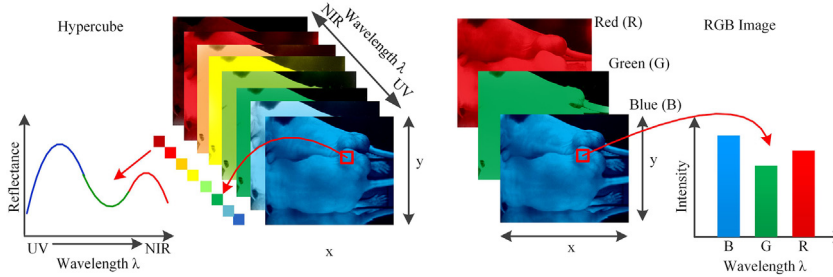

FIGURE 1 Comparison between hypercube and RGB image. Hypercube is three-dimensional data set a 2D image on each wavelength. The lower left is the reflectance curve (spectral signature) of a pixel in the image. RGB color image only has three image bands on red, green, and blue wavelength, respectively. The lower right is the intensity curve of a pixel in the RGB image.

can be integrated with other instruments, such as microscope, endoscope, colposcope, fundus camera, in order to meet specific imaging needs.

HSI devices work in a way that the tissue sample illuminated by the light source is projected through a front lens into entrance slit which only passes light from a narrow line (Fig. 2). After collimation, a dispersive device (such as prism, grating, etc.) splits the light into a series of narrow spectral bands that are then focused onto a detector array. Slit width controls the amount of light entering the spectrograph. In this way, for each pixel interval along the line defined by the slit, a corresponding spectrum is projected on a column of the detector array. Thus, each line of the targeted area on tissue sample is projected as a 2D image onto the detector, with one spatial dimension and one spectral dimension. By scanning over the tissue specimen or moving the camera across the tissue sample in a push broom or line-scanning fashion, HSI camera collects 2D images for adjacent lines, creating a hypercube with two spatial dimensions and one spectral dimension.

HSI system has been combined with many other techniques, such as laparoscope [32], colposcope [33], fundus camera [34–36], and Raman scattering [37], in order to utilize advantages of both imaging instrument and provide more useful information for disease diagnosis and treatment. The most common combination is with microscope [38–46] or confocal microscope [47], which has been proved useful in the investigation of the spectral properties of tissue.

Epifluorescence microscope and imaging spectrometer are often coupled to form an HSI microscope. Tsurui et al. [38] proposed an HSI system which mainly consisted of an epifluorescence microscope and an imaging spectrometer to capture and classify complete fluorescent emission spectra from multiple fluorophores simultaneously from typical biomolecular samples, identify the location of the emission, and build libraries to enable automatic analysis in subsequent acquisitions. Schultz et al. [48] developed a prototype HSI microscope with a standard epifluorescence microscope and an imaging spectrograph which permits the capture and identification of different spectral

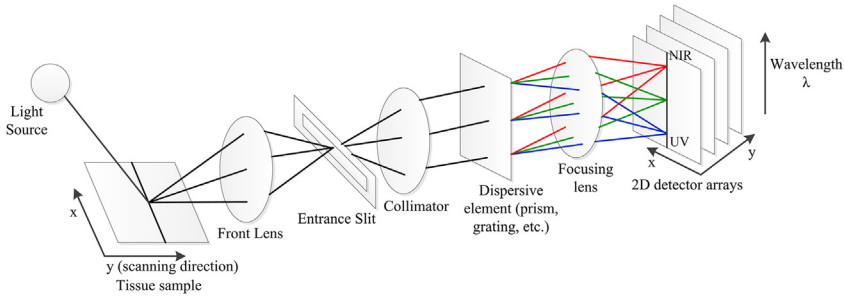

FIGURE 2 Schematic diagram of a push broom hyperspectral imaging system. *NIR*, Near-infrared.

signatures present in an optical field during a single-pass evaluation, including molecules with overlapping but distinct emission spectra. However, the major limitation with these systems are small fields of view (FOVs), thus requiring image tiling for tissue section imaging. In order to increase the FOV, Constantinou et al. [49] integrated a confocal scanning macroscope with a prototype HSI mode, called hyperspectral macroscope (HSM) which allows image acquisition of entire microscope slides in a single FOV, avoiding the need to tile multiple images together. In confocal fluorescence microscopy, the scanning mechanism of HSM imaging must trade off between image signal-to-noise ratio and photobleaching.

4. Image analysis

Image analysis enables the extraction of diagnostically useful information from large amount of medical hyperspectral data set at the tissue, cellular, and molecular levels and is therefore critical for disease screening, diagnosis, and treatment. Hypercube with high spatial and spectral resolution may potentially contain more diagnostic information. However, high spatial and spectral dimension also makes it difficult to perform automatic analysis of hyperspectral data. In particular, it is complex in many aspects: (1) high data redundancy due to high correlation in the adjacent bands, (2) variability of hyperspectral signature, (3) curse of dimensionality [50]. With abundant spatial and spectral information available, advanced image classification methods for hyperspectral data sets are required to extract, unmix, and classify relevant spectral information. The goal is not only to discriminate between different tissues (such as healthy and malignant tissue) and provide diagnostic maps but also to decompose mixtures by spectral features, and correlate biomarkers with disease states. Although hyperspectral image analysis methods have been intensively investigated in the remote sensing area, their development and applications in medical domain lag far behind. The relationships between spectral features and underlying biomedical mechanisms are not well understood. The basic steps for hyperspectral image analysis generally involve preprocessing, feature extraction and feature selection, classification, or unmixing.

4.1 Data preprocessing

HSI preprocessing mainly involves data normalization and image registration. Gaussian filter was also used in the literature to smooth spectral signatures and reduce the noise effect [51].

Data normalization converts or normalizes hyperspectral radiance observations to reflectance [52,53] or absorbance [54,55] values that described the intrinsic properties of biological samples. Such normalization also reduces system noise, and image artifacts arising from uneven surface illumination or

large redundant information in the subbands of hyperspectral imagery, and better prepares data for further analysis. Two most commonly used normalization methods are:

(1) *Reflectance* [52,53]: Two auxiliary data were acquired during the experiments: the radiance of a reference white board placed in the scene and the dark current measured by keeping the camera shutter closed. The raw data was then corrected using the following equation:

$$I_{ref} = \frac{I_{raw} - I_{dark}}{I_{white} - I_{dark}} \tag{1}$$

where I_{ref} is the calculated reflectance value, I_{raw} is the raw data radiance value of a given pixel, and I_{dark} and I_{white} are the dark current and the white board radiance, respectively.

(2) *Optical density* [54,55]: It is a way of eliminating the instrument response profile in the multispectral image. This is usually accomplished by taking the ratio of the sample images (S) with respect to a reference multispectral image (R). The reference material is of known and preferably constant reflectance across the spectral range of interest. The optical density at each pixel is $X = \log R - \log S$, the reference material provides a measure of the instrument response function and therefore the method effectively ratios out the instrument response function from the resultant optical density image set X.

Image registration is to find a geometric transformation of multiple images of the same scene taken at different wavelengths. The correspondence between the images is maximized when an image pair is correctly aligned. To obtain accurate spectral information for each pixel, image registration may be necessary to spatially align all spectral band images within one hypercube or between different hypercubes. Kong et al. [51] utilized mutual information (MI) as a metric for searching the offset of the band images along the horizontal axis, and an image pair with maximum MI shows the best match between a reference image and an input image. Each band image was spatially coregistered to eliminate the spectral offset caused during the image capture procedure. Panasyuk et al. [56] performed image registration as a preprocessing step to account for slight motion during the imaging of anesthetized mice. Lange et al. [57] developed an elastic image registration algorithm to match reflectance and fluorescence images to compensate for soft tissue movement during the acquisition of reflectance and fluorescence image cubes. A detailed description of image registration algorithms is beyond the scope of this chapter. Interested readers may check relevant references to identify a suitable approach for a specific study.

4.2 Feature extraction and selection

The goal of feature extraction and selection is to obtain the most relevant information from the original data and represent that information in a lower dimensionality space. For hyperspectral data set, a larger number of spectral bands may potentially make the discrimination between more detailed classes possible, but due to the curse of dimensionality, too many spectral bands used in classification may decrease the classification accuracy [50]. Moreover, not all of the intensity measured at a given wavelength is important for understanding the underlying characteristics of biological tissues [17], since the reflectance or fluorescence features of biological tissues is wavelength dependent. Therefore, it is important to perform feature extraction and selection to extract the most relevant diagnostic information and process the data set more efficiently and accurately. In hyperspectral data set, each pixel can be represented in the form of an N-dimensional vector where N is the number of spectral bands. Such pixel-based representation has been widely used for hyperspectral image processing task. This method treats hyperspectral data as unordered listings of spectral measurements without particular spatial arrangement [58], which may result in a salt-and-pepper look for the classification map. Therefore, feature extraction methods incorporating both spectral information and spectral information has been investigated intensively in the remote sensing area to improve classification accuracy. Recent advances of spatial-spectral classification have been summarized by Fauvel et al. [59].

To exploit the information in these data sets effectively, dimensionality reduction methods are required to reduce the dimensionality of the data sets and handle highly correlated bands. The most widely used dimensionality reduction method for medical hyperspectral data set analysis is principle component analysis (PCA), which reduces redundant information in the bands of hyperspectral imagery while preserving as much of the variance in the high-dimensional space as possible. PCA of hyperspectral image data was able to highlight relative distributions of different molecular component mixtures [32,60], identify key discriminative features [19,61], or estimate spectrum in the spectroscopic data [62]. PCA is optimal in the sense of minimizing the mean square error. However, PCA transforms the original data to a subspace spanned by eigenvectors, which makes it difficult to interpret the biological meaning after transformation.

Several PCA variants, such as minimum noise fraction (MNF) and independent component analysis are also used for dimensionality reduction. MNF transform is essentially two cascaded PCA transformations for reducing the spectra dimensionality and separating noise from the image data [63]. Other feature selection methods include feature ranking by Pearson's correlation, annova test, MI, etc. and optimal feature subset selection with wrappers, filters, and embedded methods [64].

4.3 Classification

Hyperspectral image classification methods applied in medical area mainly includes pixel and subpixel-based classification. Pixel-wise classification can be parametric or nonparametric. Parametric classifiers generally assume the normal distribution for the data, which is often violated in practice [65]. Nonparametric methods, such as support vector machines (SVMs) [51,66–74] and artificial neural networks [52,75–77] are widely used in the medical hyperspectral image processing.

4.3.1 Support vector machines

SVM is a kernel-based machine learning technique which has been widely used in the classification of hyperspectral images [66,78,79]. Due to its strong theoretical foundation, good generalization capability, low sensitivity to the curse of dimensionality [80], and ability to find global classification solutions, SVMs is usually preferred by many researchers over other classification paradigms. SVM has been proved to perform well for classifying hyperspectral data [66]. In the processing of medical hyperspectral data, SVM has also been explored for various classification tasks. Melgani et al. [66] investigated the effectiveness of SVMs in the classification of hyperspectral remote sensing data. It was found that SVMs were much more effective than radial-basis function (RBF) neural networks and the KNN classifier in terms of classification accuracy, computational time, and stability to parameter settings. Kong et al. [51] implemented an SVM-based spectral signature classification method. The Gaussian RBF kernel was used in the classification algorithm. The SVM parameters are trained from 100 samples chosen randomly from each of the normal and tumor classes. For testing, 2036 (normal) and 517 (tumor) samples are used for validation. Experimental results show that the spatial filtering enhanced the performance, which resulted in an overall accuracy of 86% while the use of the original data had an accuracy of 83%.

In our group, we used SVMs for various tissue classifications. Akbari et al. has applied SVMs to perform classification tasks in several different medical applications. In Ref. [69], they extracted and evaluated the spectral signatures of both cancerous and normal tissue and used least square SVMs to classify prostate cancer tissue in tumor-bearing mice and on pathology slides. In Ref. [70], they created a library of spectral signatures for different tissues and discriminated between cancerous and noncancerous tissues in lymph nodes and lung tissues using SVMs. In Ref. [71], Akbari at al constructed a library of spectral signatures from hyperspectral images of abdominal organs, arteries, and veins, and then differentiated between them using SVMs. In Ref. [72], they utilized least squares kernel SVMs to classify normal tissue and tumor based on their standard deviation and normalized difference index of spectra signature.

4.3.2 Artificial neural networks

Neural network is another supervised classification method that has been adopted by many researchers [65,75–77], due to its nonparametric nature, arbitrary decision boundary, etc. Multilayer perceptron is the most popular type of neural network in image classification [65], which is a feed-forward network trained by the back-propagation algorithm. Monteiro et al. [52] implemented both single-layer perceptron and multilayer perceptron networks as supervised classifiers. The multilayer perceptron notably generated the clearest visualization of the calendar's number under the blood, while the single-layer perceptron was also able to learn a good visualization but the output presented more noise.

Other supervised classification methods are based on distance similarity measure such as spectral information divergence (SID), spectral angle mapper (SAM), and Euclidean distance measure.

4.3.3 Spectral Information Divergence

SID models the spectrum of a hyperspectral image pixel as a probability distribution in order to measure the discrepancy of probable behaviors between two spectra. Monteiro et al. [81] used the SID technique to segment pathological white blood cells (WBCs) into four components: nucleus, cytoplasm, erythrocytes, and background. The SID method could not only distinguish different parts with similar gray values, e.g., in the case of cytoplasm and erythrocyte, but also segment WBCs accurately in spite of their irregular shapes and sizes.

4.3.4 Spectral Angle Mapper

SAM determines the spectral similarity by calculating the angle between the spectra and treating them as vectors in a space with dimensionality equal to the number of wavelengths. Martin et al. [82] employed SAM algorithm to map the spectral similarity between image spectra and cluster spectra in order to perform supervised classification, and they found that SAM disregarded specific surface irregularities of the vocal cords that naturally led to inhomogeneous reflections in every patient. Li et al. [83] used the SAM algorithm to identify the nerve fibers from the molecular hyperspectral images of nerve sections according to the difference of the spectral signatures of different parts. Sorg et al. [40] chose the spectral angle mapping technique for pixel classification to distinguish spectrally similar fluorescent species because only knowledge of the target spectrum was required, and SAM was insensitive to scaling of the amplitude of the measured emission spectrum in the ideal case.

4.3.5 Spectral unmixing

One of the confounding factors in analyzing hyperspectral images is that the spectra at many pixels are actually mixtures of the spectra of the pure constituents. Spectral unmixing is a subpixel analysis method, which decomposes a mixed pixel into a collection of distinct spectra, or endmembers, and a set of

fractional abundances that indicate the proportion of each endmember [84]. Spectral unmixing algorithms include supervised or unsupervised methods. Supervised spectra unmixing relies on the prior knowledge about the reflectance patterns of candidate surface materials, while unsupervised unmixing aims to identify the endmembers and mixtures directly from the data without any user interaction [85]. Many unmixing algorithms that were commonly used in remote sensing have been explored in MHSI. Berman et al. [86] implemented an unmixing method, i.e., iterated constrained endmembers (i.e., ICE), for hyperspectral data of cervical tissue with the aim to identify cellular and morphological features as a prelude to construct a library of biologically interpretable endmembers. In another study, Constantinou et al. [49] applied linear unmixing to hyperspectral images in order to remove autofluorescent signal contribution. It was considered that hyperspectral spatial spectrum is a combination of autofluorescence spectrum and other fluorescence spectrum of object tissues such as tumors. By decompositing the acquired spectra into different ones, autofluorescent signals can be removed or reduced. Sorg et al. [40] performed spectral mixture analysis by utilizing a spectral angle mapping technique in order to classify pixels as expressing green fluorescent protein (GFP) or Red fluorescent protein (RFP). Begelman et al. [87] addressed the problem of fully automated decomposition of hyperspectral images for transmission light microscopy using a blind source separation (BSS) algorithm. The BSS method was based on the sparsifying transformation of observed images and the Newton optimization procedure. That method was verified on hyperspectral images of biological tissues.

5. Medical applications

HSI has been used for medical diagnosis and image-guided surgery. It is able to deliver nearly real-time images of biomarker information, such as oxyhemoglobin and deoxyhemoglobin, and provide assessment of tissue pathophysiology based on the spectral characteristics of different tissues [56]. HSI has been applied to the diagnosis of hemorrhagic shock [88,89], the assessment of peripheral artery disease [90], early detection of dental caries [91], fast characterization of kidney stone types [77], detection of laryngeal disorders [82], and so on. An overview of the wide use of HSI in medical applications is given in Table 1.

5.1 Disease diagnosis

HSI has tremendous potential in disease screening, detection, and diagnosis because it is able to detect biochemical changes due to disease development such as cancer cell metabolism [19,33,106]. In the literature, a variety of studies have used HSI techniques to augment existing diagnostic methods or to provide more efficient alternatives. In this section, diseases, such as different types of cancer, ischemic tissue, skin burn, retinal disease, diabetes, kidney disease, and so on, are investigated by various HSI systems.

TABLE 1 Summary of representative hyperspectral imaging systems and their medical applications.

References	Spectral range (nm)	Spectral resolution (μm/pixel)	Detector	Dispersive device	Acquisition mode	Measurement mode	Application
Afromowitz et al. [14]	400–1100	–	Si CCD	Filter wheel	Staring	Reflectance	Burn wounds
Ferris et al. [19]	200–700	~5	CCD	Filter wheel	Staring	Fluorescence and reflectance	Cervical neoplasia
Benavides et al. [33]	330–480	5	CCD	Filter wheel	Staring	Fluorescence and reflectance	Cervical cancer
Shah et al. [39,92]	530–680	12	CCD	Prism	Push broom	Transmission	Cutaneous wound
Bambery et al. [93]	5,000–10,526	11	HgCdTe	–	FTIR	Reflection	Cervical pathology
Greenman et al. [94]	500–600	–	CCD	LCTF	Staring	Reflectance	Diabetic foot
Sorg et al. [40]	400–720	–	CCD	LCTF	Staring	Fluorescence	Tumor hypoxia and microvasculature
Kong et al. [95]	440–640	1–2	CCD; ICCD	AOTF	Staring	Fluorescence and reflectance	Skin cancer
Cancio et al. [88]	500–600	–	CCD	LCTF	Staring	Reflectance	Hemorrhagic shock

Dicker et al. [96]	365–800	~1	CCD	Prism	Push broom	Transmission	Melanoma
Randeberg et al. [97,98]	400–1000; 900–1700; 950–2500	5	Si CCD; InGaAs; HgCdTe	Grating	Push broom	Reflectance	Skin bruises
Johnson et al. [99]	450–700	~1	FPA	CGH	Snapshot	Reflectance	Ophthalmology
Panasyuk et al. [56]	450–700	–	CCD	LCTF	Staring	Reflectance	Breast cancer
Zuzak et al. [32]	650–1100	–	FPA	LCTF	Staring	Reflectance	Laparoscopic surgery
Akbari et al. [100]	400-1000; 900–1700	5	CCD; InGaAs	PGP	Push broom	Reflectance	Intestinal ischemia
Akbari et al. [72]	1000–2500	6.29	HgCdTe	PGP	Push broom	Reflectance	Gastric cancer
Kester et al. [101]	450–650	4–10	CCD	Prism	Snapshot	Reflectance	Endoscope
Larsen et al. [63]	410–1000	–	Si CCD	Grating	Push broom	Reflectance and fluorescence	Atherosclerosis
Yudovsky et al. [102]	400–720	–	CCD	LCTF	Staring	Reflectance	Diabetic foot
Akbari et al. [69]	450–950	2	CCD	LCTF	Staring	Reflectance	Prostate cancer

Continued

TABLE 1 Summary of representative hyperspectral imaging systems and their medical applications.—cont'd

References	Spectral range (nm)	Spectral resolution (μm/pixel)	Detector	Dispersive device	Acquisition mode	Measurement mode	Application
Martin et al. [82]	390–680	–	CCD	Grating	Push broom	Reflectance	Laryngeal disorders
Mitra et al. [103]	650–750	–	CCD	LCTF	Staring	Fluorescence and reflectance	Cholecystectomy
Renkoski et al. [104]	400–640	–	CCD	Filter wheel	Staring	Fluorescence and reflectance	Ovarian cancer
Rosas et al. [105]	1000–2400	7	HgCdTe	LCTF	Staring	Reflectance	Pharmaceutical
Usenik et al. [91]	900–1700	5	InGaAs	AOTF	Staring	Reflectance	Dental caries
Guan et al. [81]	550–950	2–5	CCD	AOTF	Staring	Transmission	Leukocyte pathology
Li et al. [83]	550–1000	~2	CCD	AOTF	Staring	Transmission	Nerve fiber identification
Kumar et al.	2,500–11,111	–	HgCdTe	–	FTIR	–	Breast cancer

CCD, Charge-coupled device; *Si CCD*, Silicon CCD; *LCTF*, Liquid crystal tunable filter; *FPA*, Focal plan array; *CGH*, Computer-generated hologram.

5.1.1 Cancers

The rational for cancer detection by optical imaging lies on the fact that biochemical and morphological changes associated with lesions alter the absorption, scattering, and fluorescence properties; therefore optical characteristics of tissue can in turn provide valuable information for cancer screening and detection. For example, optical absorption can reveal angiogenesis and increased metabolism activity by quantifying the concentration of hemoglobin and oxygen saturation of hemoglobin [107]. Kortum et al. [108] used optical spectroscopy to detect neoplasia and reported that (1) the increased metabolic activity affects mitochondrial fluorophores and changes the fluorescence properties in precancer tissue, and (2) fluorescence and reflectance spectra contain complementary information that was useful for precancer detection.

Compared to optical spectroscopy which measures tissue spectra point by point, HSI is able to capture images of a large area of tissue and has exhibited great potential in the diagnosis of cancer in the cervix [19,33,109,110], breast [56,111], colon [41,43,74,112−117], gastrointestine [118,119], skin [96,120], ovarian [104], urothelium [121], prostate [69], esophageal [122], trachea [123], oral tissue [20,30,124,125], tongue [53], lymph nodes [126], and brain [127]. HSI cancer studies have been performed in the following major aspects: (1) recognizing protein biomarkers and genomic alterations on individual tumor cells in vitro [128]; (2) analyzing the morphological and structural properties of cancer histological specimens to classify the cancer grades; (3) examining the tissue surface to identify precancerous and malignant lesions in vivo; (4) measuring the tissue blood volume and blood oxygenation to quantify the tumor angiogenesis and tumor metabolism. The following section briefly summarizes the research works that have been performed for certain types of cancers without covering all the abovementioned cancers.

5.1.1.1 Cervical cancer

Cervical cancer was once one of the most common causes of cancer death in American women. Pap smear tests, the current screening method for cervical cancer, are based on optical techniques and offer an effective method for identifying precancerous and potentially precancerous changes in cervical cells and tissue [129]. However, Pap smear test has been reported to have false positive rate of 15%−40%. It has also been reported that in normal cervical tissue, collagen and cross-links exhibit bright fluorescence in the stroma over a wide range of excitation wavelengths; while in cervical precancers, stromal fluorescence is strongly decreased [110]. Studies also showed that both reflectance and fluorescence spectroscopy can detect increased angiogenesis which accompanies precancer [130].

In vivo study: Combination of fluorescence and reflectance imaging has been shown to be able to interrogate the cervix tissue in vivo. Ferris et al. [19] performed a clinical study on a diverse population of women with varying

disease and nondisease states using an HSI system which covered the UV and vis to measure tissue fluorescence and reflectance of the cervical epithelium on the ectocervix. This system employs both fluorescence and reflectance tissue excitation with a multichannel spectrograph capable of hyperspectral resolution of about 5 nm and spatial resolution of the ectocervix of about 1 mm. They showed that the system could discriminate high-grade cervical lesions from less severe lesions and normal cervical tissue, and could detect cervical cancer precursors at a rate greater than that obtained by a simultaneously collected Pap smear. It was concluded that fluorescence and reflectance mapping of cervical neoplasia may have some value as a colposcopy adjunct.

Later, multispectral digital colposcope (MDC) was built to incorporate multispectral imaging with colposcope by Benavides et al. [33] in order to measure the autofluorescence and reflectance images of the cervix. It was concluded that MDC could provide significant diagnostic information for discrimination between cervical intraepithelial neoplasia lesions from normal cervical tissues, and that excitation wavelengths across the spectral range of 330−360 nm and 440−470 nm appeared important in cervical cancer diagnosis.

Histology study: Besides the in vivo studies, HSI on cervical cancer histology slides also showed promising results. Siddiqi et al. [109] successfully improved the overall efficiency and objectivity in Pap test diagnosis by utilizing an HSI system coupled with microscope to identify normal, low-grade, and high-grade H&E-stained cervical cells on TriPath liquid−based Pap test slides, squamous cell carcinoma cells as well as atypical squamous cells based on their unique spectra profiles. It was found that cervical cells with varying degree of dysplasia demonstrated different spectra, which could be the result of the quantity and organization of the chromatin. It was also found that H&E and Pap stain were designed only for visual spectrum, and that the use of infrared and ultraviolet spectral range may further enhance the efficacy of HSI. Wood et al. [131] employed FTIR to collect spectra of glandular and squamous epithelium, and of the cervical transformation from H&E-stained cervical samples. They performed multivariate statistical analysis of the FTIR spectra to distinguish different tissue types and found that the amide I and II regions (1740−1470 cm^{-1}) to be very important in correlating anatomical and histopathological features in tissue to spectral clusters.

5.1.1.2 Breast cancer

Breast cancer is the first leading cause of cancer death in American women [132]. An inadequate supply of oxygen in tumor cells leads to hypoxia, which has been shown to be of prognostic value in clinical trials involving radiation, chemotherapy, and surgery.

In vivo study: Sorg et al. [40] applied HSI to acquire serial spatial maps of blood oxygenation in terms of hemoglobin saturation at the microvascular level on the mouse mammary carcinoma in vivo. RFP was used to identify mouse mammary carcinoma cells while hypoxia-driven GFP was used to

identify the hypoxic fraction. Their studies may improve the treatment and protocols to address or exploit tumor behavior.

Histology study: H&E-stained histopathology imagery was analyzed with multispectral imaging by Boucheron et al. [111]. They acquired multispectral images with 29 spectral bands, spaced 10 nm within the range of 420−700 nm, from 58 H&E-stained breast cancer biopsy samples, and then classified the nuclei of breast cancer cells with the multispectral image bands, or the constructed RGB imagery, or single image bands. They found that multispectral imagery for routine H&E-stained histopathology provided minimal additional spectral information for pixel-level nuclear classification task than standard RGB imagery did. However, their result was limited to the classification of nuclei in breast histology within the spectral range of 420−700 nm with small number of wavelength bands. Kuma et al. applied FTIR on histopathological specimens of breast cancer with different histological grades. FTIR spectral changes close to and far from carcinoma was reported. PCA analysis is performed to analyze the data. Their preliminary study suggested that FTIR spectral features present in the 1700−1600 cm^{-1} could be used as spectral markers for identification of cancer-induced modifications in collagen.

5.1.1.3 Skin cancer

Two types of skin cancer have been investigated using MHSI: melanoma and Kaposi's sarcoma (KS). Melanoma is the most life-threatening form of skin cancer, which is responsible for about 75% of skin cancer death in 2012 [132].

In vivo human study: Hattery et al. [120] built a six-band multispectral near-infrared (NIR) imaging system to identify thermal signatures of blood volume on patients with KS and starting antiangiogenesis therapy. Results showed that relative spatial tissue blood volume and blood oxygen saturation values could be used as indicators of tumor angiogenesis and tumor metabolism (see Fig. 3).

Histology study: Dicker et al. [96] applied hyperspectral analysis to search for spectral differences between benign and malignant dermal tissue in routine H&E-stained specimens. In the study, the spectral differences could be

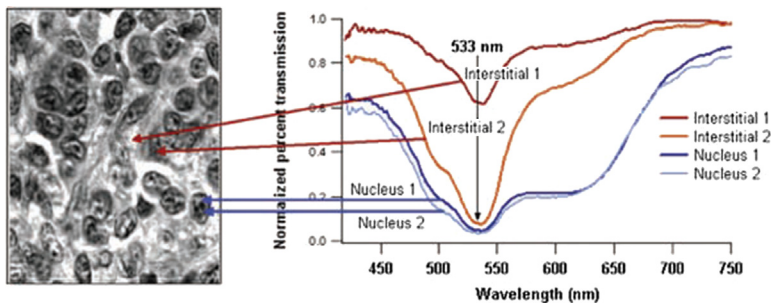

FIGURE 3 A gray scale image of a melanoma lesion showing the transmission spectra in the nuclear and interstitial areas.

objectively identified providing that staining time and section thickness were controlled. KS is a highly vascularized tumor that causes cutaneous lesions.

5.1.1.4 Head and neck cancer

Head and neck cancer (HNC) occurs in the head or neck region, including lip, oral cavity, nasal cavity, oropharynx, hypopharynx, and larynx, etc. Most of the HNCs are squamous cell carcinomas that originate from the epithelial region; therefore HSI with limited penetration depth is possible to detect the cancerous tissue.

Clinical trial: Oral cancer is a subtype of HNC located in the oral cavity, which is commonly examined by visual inspection and palpation of the mouth. However, this visual screening method depends heavily on the experience and skills of physicians. Roblyer et al. [30,124] reported the use of a multispectral digital microscope (DMD) for the detection of oral neoplasia in a pilot clinical trial. The proposed DMD was a multimodal imaging method which combines the fluorescence, narrow-band (NB) reflectance, and orthogonal polarized reflectance (OPR) modes. They observed decreased blue/green autofluorescence and increased red autofluorescence in the lesions and increased visibility of vasculature with NB and OPR imaging.

Histology study: In our group, Akbari et al. [70] imaged pathological slides using a hyperspectral camera and reported the detection of HNC metastasis with promising sensitivity and specificity. Liu et al. [53] measured and analyzed the reflectance spectra of human tongue noninvasively.

5.1.1.5 Colon cancer

Colon cancer, also known as colorectal cancer, is a malignant disease of the colon or rectum, or appendix, and is the third leading cause of cancer death for both men and women [132]. Pathological analysis is the basis of cancer diagnosis and treatment. The malignant tumor leads to considerable variation in nuclei size and shape, so traditionally, pathologists examine the specimens under microscopes and make judgments based on the deviations in the cell structures, change in the distribution of the cells across the tissue under examination. However, this process is time-consuming, subjective, and inconsistent due to inter- and intraobserver variations [133]. To overcome these problems, MHSI has been applied to discriminate cell types and tissue patterns based on pathology slides.

Histology study: Masood and colleagues explored a series of research problems for classification of hyperspectral colon biopsy images. First, they performed morphological analysis of gland nuclei cells and classified them into normal and malignant classes based on the shape, size, orientation, and other geometrical attributes of the cellular components. From this, they concluded that HSI has enough discriminatory power to distinguish normal and malignant biopsy tissue [41]. Second, they selected a single band which was considered to contain sufficient textural information, classified colon biopsy samples into benign and malignant classes based on the textural

information extracted from the single band, and achieved a reasonable classification result [74,116]. Third, they compared the classification result of a single band with 3D spectral/spatial analysis, and the former achieved comparable accuracy for SVM-based classification of 32 hyperspectral images of colon biopsy samples [43,117].

While Masood mainly focused on classifying colon biopsy tissue into benign and malignant types, Maggioni et al. [113] provided evidence that with a hyperspectral microscope, the H&E-stained microarray sections of colon tissue can be classified into normal, benign (adenoma), and malignant (carcinoma).

Traditional microscope has a limited field of view, therefore multiple images must be taken and tiled together to form a complete image of the entire tissue specimen, which is time-consuming and can introduce artifacts in the composite image. To address these issues, Constantinou et al. [49] developed a confocal scanning macroscope, integrated with a prototype HSI mode to detect fluorescently labeled antibodies and remove autofluorescence in paraffin-embedded, formalin-fixed tissues with linear unmixing method. The system was evaluated in xenograft tissue of a mouse model of human colonic adenocarcinoma, and the prototype MHSI had the ability of simultaneous imaging of multiple fluorescently labeled tissue-specific markers in large biological samples in a time- and cost-efficient way.

5.1.2 Heart and circulatory pathology

Heart disease continues to be the leading cause of death for both men and women in the United States. Each year, one in every four people in the United States dies of heart disease. HSI has been explored in heart and circulatory pathology both in vivo (animal and human studies) and in vitro.

In vitro study: Coronary artery disease arises from atherosclerosis through a slowly progressing lesion formation and luminal narrowing of arteries, which is a leading cause of death and morbidity worldwide [134]. Upon plaque rupture and thrombosis, cardiovascular disease such as acute coronary syndrome, myocardial infarction, or stroke is likely to happen. Thorough knowledge about the properties of both the lesion and adjacent vessel wall is required for the diagnosis of atherosclerosis and the determination of the right time for intervention, choice of treatment, and assessment of prognosis [63]. The standard method for diagnosis and evaluating atherosclerosis is angiography, which is limited to the detection of stenotic plaques [63]. Reflectance and fluorescence spectroscopies have been explored as diagnostic tools for atherosclerosis, such as distinguishing fibrous plaque from healthy arterial wall [135], the identifying atherosclerotic regions in arteries [136], and superficial foam cells in coronary plaques prone to erosion in vivo [137]. However, it was observed that most of the advanced lesions had a central region surrounded by an outer rim or shoulder-region of the plaque, which is considered a weak spot in vulnerable lesions [63]. The spatial variation of

plaques makes it difficult for conventional single-point spectroscopic measurements to classify a plaque correctly. HSI holds great promise for diagnosis of atherosclerosis by probing a large area of tissue under investigation and providing spectral information for each pixel in the area of interest. Larsen *et al.* [63] collected hyperspectral reflectance and fluorescence data from excised aorta samples in vitro using both white-light and ultraviolet illuminations. Plaque features such as lipids and calcifications could be identified from white-light reflectance, and UV-excited fluorescence hyperspectral images, and HSI was shown to identify the complexity and large heterogeneity of such plaques as compared to the histology.

In vivo study: Peripheral arterial disease (PAD) involves the atherosclerotic occlusion of the arterial circulation to lower extremity [138], which may lead to rest pain, lower extremity ulceration, and even limb amputation [90]. Effective diagnostic and prognostic technologies are necessary for earlier detection and treatment to avoid unnecessary complications and interventions; however, traditional methods such as ankle-brachial index, Doppler waveform analysis, and segmental limb pressure, etc. did not provide high specificity and sensitivity for prediction of healing of tissue loss in PAD patients [90]. HSI has the capacity of noninvasively measuring oxyhemoglobin and deoxyhemoglobin concentrations to create an anatomic oxygenation map [139,140]. Chin *et al.* [90] scanned patients with and without PAD with visible HSI system and acquired the concentration of oxyhemoglobin and deoxyhomoglobin. Experiments showed that HSI might be useful in detecting differences in oxygenation levels in the lower extremities of patients with and without PAD. Their data also suggested that HSI may be a useful tool for the diagnosis and evaluation of patients with PAD.

5.1.3 Retinal diseases

The delicate nature of the eye usually precludes invasive biopsy or mechanical access to the retina, therefore current diagnosis of retinal disease relies strongly upon optical imaging methods [141]. HSI system is usually integrated with a fundus camera to enable optical imaging of the eyes. Early in 1999, Cohen et al. [141] reported the use of HSI to map wavelength-resolved reflectivity across a 2D scene in order to quantify retinal images and hence offer possibility for both early detection as well as monitoring of the effectiveness of therapy. Khoobehi et al. [142] attached a fundus camera to an HSI for monitoring relative spatial changes in retinal oxygen saturation. The integrated system can be adapted to measure and map relative oxygen saturation in retinal structures and the optic nerve head (ONH) in nonhuman primate eyes. Hirohara et al. [34] measured the intensities of different wavelengths of light that were transmitted through an artery, vein, and the area surrounding these vessels and reflected out. A hyperspectral fundus imaging camera was used to capture and analyze the differential spectral absorptions of the vessels.

Johnson et al. [99] developed a snapshot HSI system with no moving parts or narrow-band filters in order to perform functional mapping of the human retina. The hemoglobin spectral signatures provide both qualitative and quantitative oxygen saturation maps (see Fig. 4) for monitoring retinal ischemia from either systemic disease such as diabetes or from localized retinal arterial and vascular occlusions, the leading causes of untreatable blindness. Fig. 4 shows a 12-deg image of the optic disk for two healthy volunteers. The results show a clear distinction between veins, arteries, and background. Regions within vessel capillaries agree well with the 30%−35% oxygen saturation difference expected for healthy veins and arteries. 32−35 The saturation for most of the background spatial locations in between the capillary regions shows a tendency to be within the 90%−100% regime. This is consistent with the subjects being healthy [99]. This system is capable of

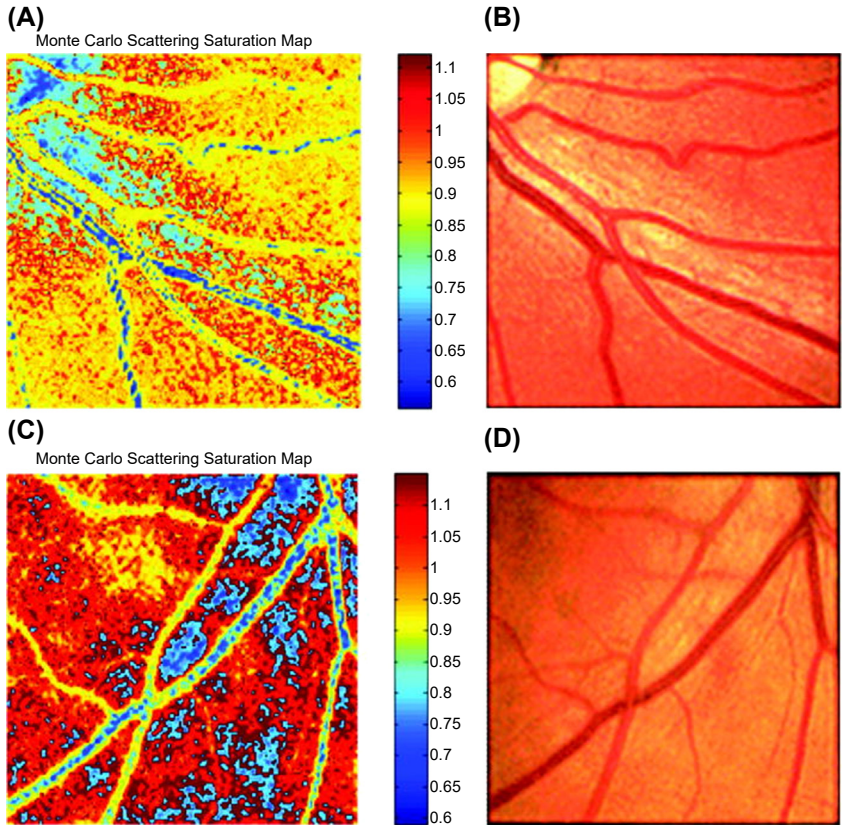

FIGURE 4 Spatial oxygen saturation maps. (A) Healthy male (29 years old) oxygen saturation map. Vascular separation from the background is seen as well as reasonable saturation values for veins versus arteries. (B) Zero-order color image. (C) Healthy male (58 years old) oxygen saturation map. (D) Zero-order color images [99].

acquiring a complete spatial-spectral image cube of 450–700 nm with 50 bands in ~3 ms and without motion artifacts or pixel misregistration. The approach is ideal for exploring the potential for this retinal application since the eye is constantly moving and often requires snapshot camera operation.

Age-related macular degeneration (AMD) is a major cause of blindness in the elderly, and the prevalence of the disease increases exponentially with every decade after 50 years [143]. Cell protein cytochrome c has been identified as a key signaling molecule in degeneration processes and apoptosis. Schweizer et al. [46] developed an HSI system to collect spectroscopic data which provided information about the oxidative state of cytochrome c during oxidative stress for detection of AMD. Fawzi et al. [35] applied CTIS to quantify the macular pigment (MP) in a group of healthy eyes in vivo. They successfully recovered detailed spectral absorption curves for MP in vivo that correspond to physically realistic retinal distributions.

5.1.4 Diabetic foot

Diabetic foot ulceration is a major complication of diabetes, and diabetic patients have up to a 25% lifetime risk of developing a foot ulcer [144]. If untreated, diabetic foot ulcers may become infected and require total or partial amputation of the affected limb. Changes in the large vessels and microcirculation of the diabetic foot are important in the development of diabetic foot ulceration and subsequent failure to heal existing ulcers. Greenman et al. [94] used MHSI system to investigate the hemoglobin saturation ($S_{HSI}O_2$) in the forearm and foot. It was found that tissue $S_{HSI}O2$ was reduced in the skin of patients with diabetes. Khaodhiar et al. [145] carried on a clinical study on 10 type 1 diabetic patients with 21 foot ulcer sites, 13 type 1 diabetic patients without ulcers, and 14 nondiabetic control subjects. MHSI predicted diabetic foot ulcer healing with a sensitivity of 93% and specificity of 86%. Tissue oxy- and deoxyhemoglobin on the upper and lower extremity distant from the ulcer were used to quantify the tissue in the study. Yudovsky et al. [146] reviewed how HSI between 450 and 700 nm could be used to assess the risk of diabetic foot ulcer development and to predict the likelihood of healing noninvasively. Two methods were described to analyze the in vivo hyperspectral measurements. The first method was based on the modified Beer–Lambert law and produced a map of oxyhemoglobin and deoxyhemoglobin concentrations in the dermis of the foot. The second was based on a two-layer optical model of skin. It could retrieve not only oxyhemoglobin and deoxyhemoglobin concentrations but also epidermal thickness and melanin concentration along with skin scattering properties. It could detect changes in the diabetic foot and help predict and understand ulceration mechanisms. In another study, the same group [102] reported the use of a hyperspectral tissue oximetry in predicting the risk of diabetic foot ulcer formation with a sensitivity and specificity of 95% and 80%, respectively. A later study [147] found that epidermal thickening and decrease in oxyhemoglobin concentration could also be detected prior to ulceration at preulcerative sites.

5.1.5 Shock

As the body's largest and most accessible organ, the skin often manifested changes in the systemic circulation, which is important for the diagnosis of patients in shock. MHSI offers a new and exciting means of measuring both the spatial and temporal variations in skin hemodynamics.

Gillies et al. [55] evaluated the ability of MHSI to depict and quantify the cutaneous manifestations of shock using a porcine model. Shock was induced by chest trauma followed by hemorrhage. Quantitative and qualitative changes were observed in the level of skin oxygenation during shock and recovery. A mottled pattern of oxygen saturation was observed during hemorrhagic shock instead of during hypovolemic shock or following resuscitation. The study showed that noninvasive imaging of skin oxygen saturation could potentially be useful in monitoring the response of the microvasculature to shock and subsequent treatment. Variation in cutaneous blood flow distribution and hemoglobin saturation measured by MHSI may offer new insights into the pathophysiology and treatment of shock.

Skin color changes and mottling are frequently described signs of hemorrhagic shock (HEM). Cancio et al. [88] developed a noninvasive, noncontact HSI system to quantify and depict the surface tissue saturation of oxygen ($S_{HSI}O_2$) for each pixel in a region of interest (ROI). A study of 17 female pigs showed linear decreases in both mean $S_{HSI}O_2$ and OxyHb values with blood loss, which were reversed by resuscitation. HSI is a promising noninvasive and noncontact tool for quantifying changes in skin oxygenation during HEM and resuscitation.

5.1.6 Others

By recording the variations in the percentages of oxygen saturation of hemoglobin, optical methods are able to monitor the visible and NIR spectral properties of the blood. Zuzak et al. [148,149] measured the changes in the spatial distribution of regional tissue oxygenation during vascular occlusion and reperfusion. This method was able to noninvasively visualize and differentiate between normal and ischemic tissue. This approach may have a variety of applications in surgical and diagnostic procedures. In the same group, a visible reflectance HSI system was introduced to quantify the percentage of oxyhemoglobin (HbO_2) as an index of skin tissue perfusion. The HSI demonstrated (1) a significant decline in the percentage of HbO_2 in skin tissue was found when blood flow is reduced after inhibition of forearm nitride oxide synthesis and (2) restoration of HbO_2 toward basal values with improved blood flow during inhalation of nitride oxide [150]. In a clinical study [151], the same group used a visible reflectance HSI system to examine a model of vascular dysfunction involving both ischemia and reactive hyperemia during tissue perfusion. The method was based on oxyhemoglobin and deoxyhemoglobin signals from spectral images in the 525- to 645-nm region. It was able to visualize the spatial distribution of percentages of oxyhemoglobin and deoxyhemoglobin in specific skin tissue areas.

Another important application of HSI in histopathological examination of tissue is a combination of hyperspectral instrument with other techniques such as microscope, macroscope, micromachined angular filter array, or snapshot fiber bundle. Huebschman et al. [152] took the advantage of the continuous spectrum collected for each image pixel by a hyperspectral microscopy system to scan and analyze pathology tissue samples. Those samples were stained with four standard fluorochromes attached to specific antibodies typically across the wavelength range of 420−785 nm with the longest wavelength markers emitting in the spectral region where the human eye was not sensitive. Begin et al. [37] presented a wavelength-swept approach to coherent anti-Stokes Raman scattering microscopy. The system was especially well suited for experiments on thick tissue where scattering played an important role. It bridged an important gap between fundamental research microscopy tools and clinically useful instruments by combining the context of imaging with the

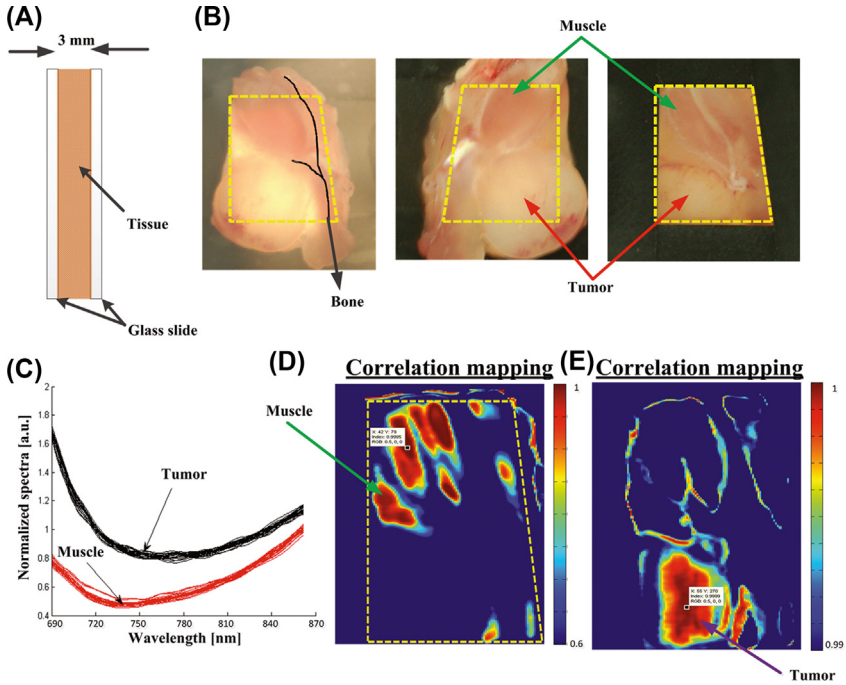

FIGURE 5 (A) Cross-section diagram of tissue sample for ADSI testing. (B) Color photographs of mouse tumor tissue sandwiched between two glass slides. The opening due to the black mask that was used for transmission imaging is marked by the yellow dashed line. The black line (left panel) indicates the location of bone embedded in the tissue. (C) Normalized spectra from regions of tumor and muscle tissue (as indicated in (B)). (D) Correlation map of data cube based on reference spectral signature related to the muscle tissue. (E) Correlation map of data cube based on reference spectral signature related to the tumor tissue [153]. *ADSI*, Angular domain spectroscopic imaging.

richness of spectroscopic information. Vasefi et al. [153] proposed an innovative hyperspectral optical imaging technology called angular domain spectroscopic imaging (ADSI) that retained submillimeter spatial resolution as well as high spectral resolution through tissue specimens up to 3-mm thick (cross-section diagram of tissue sample is shown in Fig. 5). Khoobehi et al. [154] developed an innovative snapshot HSI system which detected the whole spectrum of hemoglobin using the single light exposure capabilities of a fundus camera. It was able to record the hemoglobin signature of the retinal arteries, veins, and retina tissue. Sowa et al. [54] revealed that differences in tissue reflectance correlates with the varying degree of tissue perfusion immediately following surgical elevation of the reversed McFarlane skin flap.

5.2 Surgical guidance

The success of surgery highly depends on a surgeon's ability to see, feel, and make judgment to identify the lesion and its margins [155]. MHSI holds the potential to extend surgeon's vision at the molecular, cellular, and tissue levels. The ability of MHSI as an intraoperative visual aid tool has been explored in many surgeries.

First, MHSI could help surgeon to visualize the surgical bed under the blood. Visual inspection is critical in microsurgery. However, the inevitable presence of blood spilling over the surgical field is a large visual obstacle to a successful surgery. Therefore, NIR HSI spectrograph was utilized to visualize tissues submerged in a blood layer that could not be seen with the naked eye [52,156].

Second, MHSI could facilitate residual tumor detection [56]. Surgery remains the foundation of cancer treatment, with the central objective of maximizing removal of the tumor, without harming adjacent normal tissue. However, cancerous tissue is often indistinguishable from healthy tissue in the operating room, which leads to the high mortality rates from recurrent tumors. The rational of residual tumor detection by MHSI lies on the fact that MHSI is able to distinguish the spectral difference of normal and cancerous tissue in nearly real time during the procedure [56].

Third, MHSI could monitor the tissue oxygen saturation during surgery. Tissue blood flow or oxygenation is a positive indicator of viable tissue, which might be otherwise sacrificed when removing tumor with little guidance. HSI could monitor the tissue at a rate of three frames per second, thus could detect dynamic changes in blood flow and capture unexpected events during surgery [157].

Finally, MHSI could enable the visualization of anatomy of vasculatures and organs during surgery. MHSI has the capacity of real-time imaging, which enables the surgeon to make or confirm diagnosis and evaluate surgical therapy in an ongoing fashion in the operation room [155].

Overall, MHSI has been explored in surgery such as mastectomy [56], gallbladder surgery [158], cholecystectomy [60,103], nephrectomy [159,160], renal surgery [157,159,161–163], abdominal surgeries [71], and intestinal surgery [164]. The following section will introduce these research studies in details.

5.2.1 Mastectomy

Although approximately 45% of patients with breast cancer undergo primary surgical treatment with mastectomy. The rates of complete resection remain surprisingly low, and re-excision rates in breast lumpectomy have been reported to be as high as 40% in some studies [165]. Residual tumors were often found at the margin of the resected specimen that was not apparent to the surgeon at the time of procedure. Therefore, intraoperative assessment of residual tumor is critical for complete resection. Panasyuk et al. [56] successfully detected residual tumors of 0.5−1.0 mm intentionally left in the operative bed (see Fig. 6) during an intraoperative experiment using MHSI in a rat breast tumor model. The rat breast tumors were first exposed and imaged by MHSI, then partially resected and imaged again by MHSI. They successfully identified and differentiated tumors, blood vessels, muscle, and connective tissue by MHSI. A sensitivity of 89% and a specificity of 94% for the detection of residual tumors, comparable to that of histopathological examination of the tumor bed, were reported. With the aid of MHSI, more extensive resection and more effective biopsy locations may be identified. The complete resection of tumor tissue and

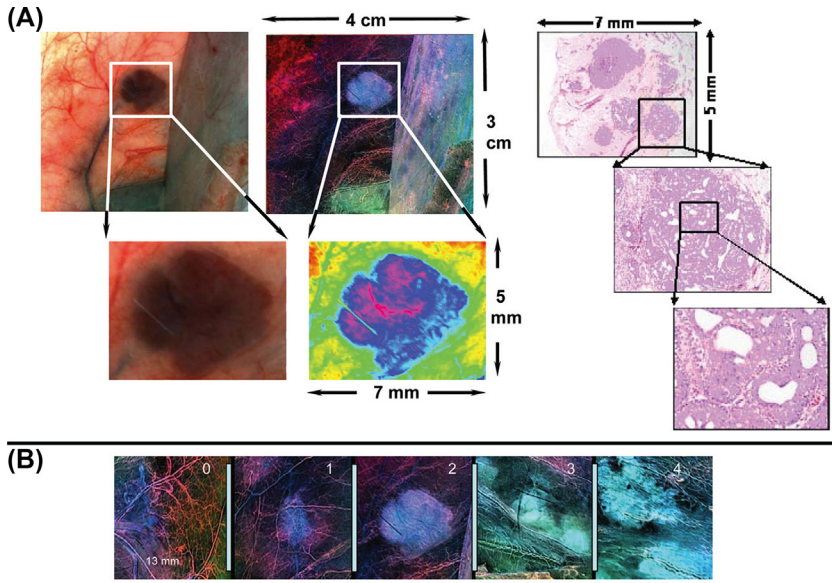

FIGURE 6 (A) Photomicroscopic and corresponding medical hyperspectral imaging image from breast tumor in situ (4 × 3 cm) (upper left and upper middle panels). Resected tumor and surrounding tissue (5 × 7 mm) was stained with hematoxylin and eosin and evaluated by histopathology after resection. Microscopic histological images with further resolution are displayed (right panels). (B) Representative examples of normal tissue (grade 0), benign tumor (grade 1), intraductal carcinomas (grade 2), papillary and cribriform carcinoma (grade 3), and carcinoma with invasion (grade 4) are represented [56].

the conservation of normal tissue may improve surgery outcome, preservation of organ function, patient satisfaction, and quality of life.

5.2.2 Gall bladder surgery

Diseases of the gallbladder, such as symptomatic gallstones and other gallbladder conditions, often require the surgical removal of the gallbladder, i.e., cholecystectomy, one of the most commonly performed surgeries in the United States. Standard surgical procedure is a closed laparoscopic cholecystectomy. The procedure involves several small incisions in the abdomen with diameters of 5−10 mm. Surgical instrument and a video camera are placed into the abdominal cavity. In this case, surgeons lost tactile feedback; and the conventional video camera through an endoscope to identify the biliary tree had limited image contrast. Therefore, Zuzak et al. [32] developed an endoscope-based HSI system to identify the anatomy and molecular content of tissue during laparoscopic surgery in swine. The study showed the utility of NIR laparoscopic HSI for noninvasive interrogation and identification of tissues based on their chemical composition in a real-time intraoperative manner and without radioactive contrast agent. They found that lipids absorbing light at 930 nm could be used as an inherent biomarker for imaging the lipid-containing bile ducts connecting the gallbladder, the location of which the surgeon need to identify before cutting during cholecystectomy. In order to help surgeons delineate the hepatoduodenal ligament anatomy to avoid causing serious harm to the biliary tree, they [60] also built a laparoscopic-capable, NIR, HSI system for intraoperative biliary imaging in a pig, which enabled surgeons to see through the hepatoduodenal ligament and visualize the anteriorly placed biliary system. They again confirmed the common duct−reflected spectra of porcine biliary structures to have a characteristic lipid shoulder at 930 nm and a strong water peak at 970 nm. Venous structures had absorption peaks at 760 nm (deoxyhemoglobin), 800 nm (oxyhemoglobin), and 970 nm (water). Arterial vessels had absorption peaks at 800 and 970 nm that would be expected for oxyhemoglobin and water. Therefore, arterial vessels, venous structures, and bile ducts can be visualized through the hepatoduodenal ligament connective tissue during closed laparoscopic procedures.

In an ex vivo tissue study, Mitra et al. [103] used both hyperspectral and fluorescence imaging to scan the biliary structure and implemented advanced spectral analysis and image processing algorithms to classify the tissue types and to identify the biliary anatomy. While fluorescence imaging provided dynamic information of movement and flow in the surgical region of interest, data from HSI allowed for identification of the bile duct (see Fig. 7) and safe exclusion of any contaminant fluorescence from tissue not part of the biliary anatomy.

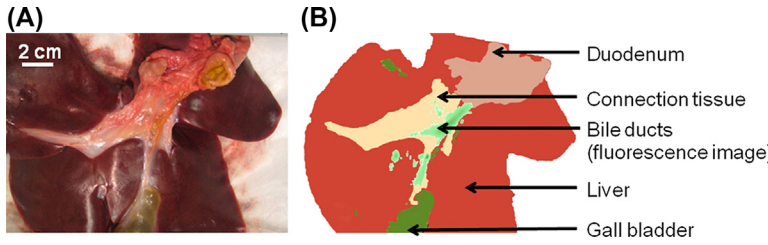

FIGURE 7 (A) Photographic image of the biliary tissue structure. (B) Classification of the biliary tissue types based on hyperspectral imaging, superimposed with the fluorescence image of the ICG-loaded microballoons. The dual-mode image clearly identifies the biliary anatomy and its relative location with respect to the surrounding tissue components.

5.2.3 Renal surgery

Although open partial nephrectomy (OPN) is considered the gold standard treatment for small (<4 cm) renal cortical tumors [166], laparoscopic partial nephrectomy (LPN) is also reported to achieve comparable long-term oncologic outcomes to those for OPN. To minimize the renal injuries caused by ischemia during the surgery, it is very important to monitor renal response to ischemia in real time. Holzer et al. [159] reported the first experiment with a digital light processing (DLP)-based HSI system covering 520−645 nm for hemoglobin to noninvasively measure renal parenchymal HbO_2 saturation and to determine the kidney response to hilar occlusion during OPN. Olweny et al. [160] recently conducted another clinical study in 18 patients utilizing a DLP-based HSI to characterize renal oxygenation during robotic-assisted LPN. The laparoscopic HSI system successfully characterized dynamic changes in renal oxygenation during LPN.

Renal hypothermia is often induced to lower the metabolic rate and to protect renal function during OPN, while warm ischemia is used for LPN because there is no efficient and effective method for inducing renal hypothermia laparoscopically [167]. Using a digital light projection HSI system, Tracy et al. [168] demonstrated that renal artery-only occlusion had a preliminary benefit to improving postoperative glomerular filtration rate after warm ischemia during LPN in a porcine model.

To make HSI practical for real-time surgical use, Zuzak et al. [157,161−163] proposed to use a DLP-based HSI system which successfully visualized chemical composition of in vivo tissues during renal surgical procedures noninvasively at near video rate. DLP HSI system used a programmable digital micromirror device (DMD) capable of generating three processed images per second and allowing the surgeon to visualize chemical changes within fractions of a second. It overcame the primary limitation of traditional wavelength scanning methods that collect data on physiological changes in minutes. To compare the capacity of DLP NIR HSI system with that of the existent LCTF NIR, Zuzak et al. [161] performed studies on a porcine kidney during renal artery occlusion. The major difference of the two systems was their light source.

Broadband light was discriminated into individual wavelengths light in the LCTF system, which was replaced by DLP light source to illuminate the tissue using predetermined spectra. It turned out that these two systems captured nearly identical spectra for the surface of the kidney. In 2010, Zuzak et al. [163] tested the robustness of DLP HSI during OPN and other surgeries. The study showed the potential of DLP HSI in surface disorders visible at or near the surface of the skin to in vivo tissue monitor during surgery.

5.2.4 Abdominal surgery

Intestinal ischemia refers to a diminished intestinal blood flow which compromises the delivery of oxygen and leads to the accumulation of deoxygenated blood and waste products. These conditions result in cell death and necrosis, leading to inflammation and ulcers. Due to the anatomical variations and unpredictable nature of surgeries, visibility is critical to correctly diagnose these problems during surgery. MHSI was able to distinguish differences among different tissues and organs and therefore allow surgeons to visualize and examine a vast area less invasively without actually removing tissue. Akbari et al. [75,100,164] reported the use of MHSI as a visual supporting tool to detect intestinal ischemia and anatomy of organs through an abdominal surgery on pigs. They identified a key wavelength range of 765−830 nm which provided the best differentiation between normal and ischemic intestine. Spleen, colon, small intestine, urinary bladder, and peritoneum were segmented based on their unique spectral signatures (see Fig. 8). It was demonstrated that MHSI could help surgeons visualize anatomy of blood vasculature and differentiate between the artery and vein during abdominal surgeries [71].

6. Discussions

Over the past 25 years, various studies have shown the exciting potentials of HSI techniques in medical applications. Based on the technology by NASA for space exploration and earth observation, HSI acquire data set which consists of

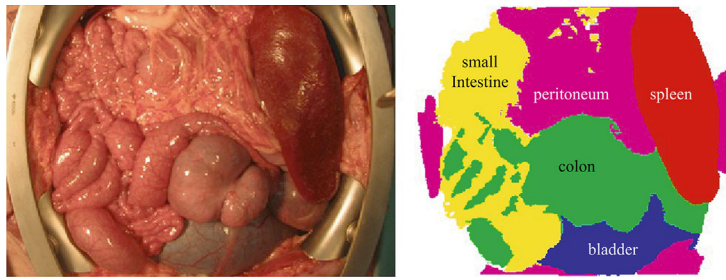

FIGURE 8 The RGB image is shown on the left side. Using the method described, the segmented image can be viewed on the right side. Spleen is shown in red, peritoneum in pink, urinary bladder in blue, colon in green, and small intestine in yellow.

two-dimensional images of spatial information and two spectral (amplitude and wavelength) dimensions at each pixel. HSI images offer more wavelength channels than RGB images taken by the ordinary color camera; therefore they may carry more useful information than RGB images. Differences that appear subtle to the human eye could be significant when looking at the detailed spectra. In addition, wavelengths, such as ultraviolet and shortwave infrared, which are invisible to the human eye, can be captured and analyzed by HSI, and can reveal information that cannot be seen by naked eyes.

MHSI is a noninvasive, and nonionizing technology, which provides a quantitative way of solving medical problems, and it may change the medical world in many ways. With the application of MHSI in exploration of anatomy, physiology, and pathology, human vision has been extended into infrared and NIR wavelength regions. Due to the noninvasive nature, MHSI can be used for optical biopsy, which is capable of performing in vivo diagnosis on tissue without the need for sample excision and processing [169]. Blood volume is generally considered to increase during angiogenesis, and changes in blood oxygenation can be correlated with tumor metabolic activity [42], therefore, MHSI can be employed to map the spatial and temporal relationship of the data, and fully grasp the significance of blood oxygen delivery and hypoxia at microvascular levels during tumor growth and angiogenesis [76]. MHSI is also able to visualize chemical contents of vessels and organs, and monitor tissue blood volume and oxygenation during surgery. The use of MHSI does not require introduction of agents, which is advantageous compared to imaging techniques that require special agents. Moreover, MHSI is able to provide us with real-time data interactively [155], which enables its usage during surgical procedures.

However, the application of MHSI can be limited because it examines only areas of tissue near the surface. The optical penetration depth is defined as the tissue thickness that reduces the light intensity to 37% of the intensity at the surface. For a typical person, the optical penetration depth is 3.57 mm at 850 nm and 0.48 mm at 550 nm. While spectral signatures have little dependence on skin temperature over the NIR, measured radiance in the thermal infrared (8−12 μm) has a strong dependence on skin temperature [170]. MHSI can also be limited by the cost of HSI imaging systems and by the ability of extracting relevant information from large data.

HSI combines spectroscopy with imaging, capturing both the spectral and spatial information of biological sample under investigation and providing spatial mapping of parameters of interest in a noninvasive manner. Spectroscopy is a point-measurement method which only measures a limited number of points so that the derived optical properties may be biased by local tissue inhomogeneities, and important diagnostic information could be missed. Pressure caused the contact probe may also affect the optical properties caused by altered local blood content, etc. [171]. Although spectroscopy has been explored extensively for probing molecular, cellular, and tissue properties

[172–174] and characterizing correlation of tissue parameters with disease state [175], such fundamental research has not been investigated vigorously in HSI. Therefore, fundamental research about biological rationale is necessary, and spectroscopy can be used to validate HSI systems. It was argued that cross talk between spatial locations could occur when extending to HSI, and the information extracted from one location might be influenced by neighboring locations [176]. Martin *et al.* [177] compared the average hyperspectral fluorescence over an area with a value obtained for one point on the tissue surface obtained by spectroscopy. It was found that the major peaks was consistent between the HIS data and spectroscopic data.

HSI technology is an indirect strategy to extract a spatial map of optical properties within the tissue, since it deduces the interaction coefficients from measurements of reflectance and transmittance [178]. This is an ill-posed inverse problem with no unique solution [179]. It is possible for two media of substantially different optical properties to yield very similar optical measurements, such as the diffuse reflectance and transmittance [178]. In practice, it is difficult to eliminate the ambiguities of matching spectral profiles with biological samples, and therefore the presence of the fundamental nonuniqueness is another limitation of HSI.

HSI can measure huge amount of spectral information from a large area of tissue. Most literature reported the feasibility of a certain MHSI application without in-depth analysis of the image data obtained. Some results may suffer from a lack of generality because the image data set are usually constrained with a specific instrument. Therefore, accessible, accurate, and up-to-date spectral database of tissues and cells for various diseases are needed in order to offer a valuable tool for better understanding and identifying disease. For example, each subtype of renal tumors such as clear cell, chromophobe, oncocytoma, papillary, and angiomyolipoma can have different morphological and molecular characteristics and thus leads to the differences in spectra signature. Therefore, a spectral library for renal tumors may be able to provide the reference spectra in order to aid the interpretation of hyperspectral images. Furthermore, advanced data mining methods are to be investigated in order to fully utilize the abundant spectral and spatial information provided by MHSI.

With the increasing integration with other techniques such as microscope, colposcope, laparoscopic, fundus camera, MSHI is becoming an essential part of medical imaging techniques, which provides important information at the molecular, cellular, and tissue levels for potential clinical use.

7. Conclusion

HSI technology acquires three-dimensional image cube with two spatial dimensions and one spectral dimension in a noninvasive manner and in real time. Each pixel in the hypercube can be characterized by a spectral curve which can range from ultraviolet to infrared region. Spatially resolved spectral obtained

by HSI provides diagnostic information about the tissue physiology, morphology, and composition. Furthermore, HSI can be easily adapted to other conventional techniques, such as microscopy, fundus camera, colposcopy, etc. As an emerging imaging technology, MHSI has been explored in a variety of laboratory experiments and clinical trials, which strongly suggested that HSI has great potential for improving accuracy and reliability in disease detection, diagnosis, monitoring, and image-guided surgery guidance.

Three major challenges confront the development and applications of HSI technology. The first challenge is the acquisition of high-resolution HSI data set in video rate. Real-time acquisition will facilitate intraoperative imaging of organs, tissues, and biomarkers of interest. Higher spectral and spatial resolution and larger database of tissue spectra will provide more spatial and spectral information and may potentially capture more subtle spectral and spatial variations of different tissue types.

The second challenge involves fast processing of the vast amount of data set acquired by HSI, including the extraction of the high-quality diagnostic information, and generation of a quantitative mapping of different tissue types as well as disease-specific endogenous substances. Advanced classification algorithms will enable better differentiation between healthy, premalignant, and malignant tissue, more precise, delineation of cancer margins for image-guided biopsy and surgery. Advanced spectral unmixing algorithms offer insight into the correlation between intrinsic biomarkers and disease states, and facilitate the identification of biomarkers by recovering subpixel compositional information.

The third challenge lies in the establishment of large spectra database for important molecular biomarkers, and all kinds of tissue types, including skin and subcutaneous tissue, ocular tissue, head/brain tissue, epithelial/mucous tissue, breast tissue, cartilage, liver, muscle, aorta, lung, and myocardium, etc. Such a database will makes it possible to distinguish not only between oxygenated and deoxygenated blood, but also different tissue types, such as bile duct and the fatty tissue surrounding it [163].

During the past two decades, HSI technology has undergone fast development in terms of hardware and systems, and has found numerous applications in medical domain. However, most MHSI only explores the UV, vis, and NIR region of light. Exploration of HSI on disease detection, diagnosis, and monitoring in mid-infrared region may bring new insights into the medical field. Moreover, combination with other imaging modalities such as preoperative positron emission tomography, and intraoperative ultrasound, can leverage the key benefits of each technique individually, overcome the penetration limitation of HSI into biological tissue [180], and broaden the application fields of HSI. In clinical settings, HSI can be easily adapted to conventional diagnostic tools such as endoscope, colposcope, etc. to meet demanding requirements by various medical applications. Multimodal imaging combining reflectance and fluorescence has the potential of revealing more information about tissue under investigation. The clinical applicability of

MHSI is clearly still in its adolescence and requires much more validation before it can be used safely and effectively in clinics. With the advancement of hardware technologies, image analysis methods, and computational power, we expect that HSI will play an important role for noninvasive disease diagnosis and monitoring, identification and quantitative analysis of cancer biomarkers, image-guided minimum invasive surgery, targeted drug delivery and tracking, and pharmaceutical drug dosage assessment.

Acknowledgments

The author thanks all his graduate students, postdoctoral fellows, and research associates for their contributions to the medical hyperspectral imaging research in the Quantitative Bioimaging Laboratory (http://www.fei-lab.org).

References

[1] W.L. Wolfe, Introduction to Imaging Spectrometers, SPIE Press, 1997.
[2] A.F.H. Goetz, Three decades of hyperspectral remote sensing of the Earth: a personal view, Remote Sensing of Environment 113 (Suppl. 1) (2009) S5−S16.
[3] C. Fischer, I. Kakoulli, Multispectral and hyperspectral imaging technologies in conservation: current research and potential applications, Studies in Conservation 51 (Suppl. 1) (2006) 3−16.
[4] H. Liang, Advances in multispectral and hyperspectral imaging for archaeology and art conservation, Applied Physics A 106 (2) (2012) 309−323 (in English).
[5] M. Govender, K. Chetty, H. Bulcock, A review of hyperspectral remote sensing and its application in vegetation and water resource studies, Water SA 33 (2) (2007).
[6] E. Adam, O. Mutanga, D. Rugege, Multispectral and hyperspectral remote sensing for identification and mapping of wetland vegetation: a review, Wetlands Ecology and Management 18 (3) (2010) 281−296 (in English).
[7] A.A. Gowen, C.P. O'Donnell, P.J. Cullen, G. Downey, J.M. Frias, Hyperspectral imaging − an emerging process analytical tool for food quality and safety control, Trends in Food Science & Technology 18 (12) (2007) 590−598.
[8] Y.Z. Feng, D.W. Sun, Application of hyperspectral imaging in food safety inspection and control: a review, Critical Reviews in Food Science and Nutrition 52 (11) (2012) 1039−1058 (in English).
[9] G.J. Edelman, E. Gaston, T.G. van Leeuwen, P.J. Cullen, M.C.G. Aalders, Hyperspectral imaging for non-contact analysis of forensic traces, Forensic Science International 223 (1−3) (2012) 28−39.
[10] D.B. Malkoff, W.R. Oliver, Hyperspectral imaging applied to forensic medicine, Proceedings of SPIE (2000) 108−116.
[11] J. Kuula, et al., Using VIS/NIR and IR spectral cameras for detecting and separating crime scene details, in: Proc. SPIE 8359, Sensors, and Command, Control, Communications, and Intelligence (C3I) Technologies for Homeland Security and Homeland Defense XI, 2012, p. 83590P.
[12] R.L. Schuler, P.E. Kish, C.A. Plese, Preliminary observations on the ability of hyperspectral imaging to provide detection and visualization of bloodstain patterns on black fabrics, Journal of Forensic Sciences 57 (6) (2012) 1562−1569.

[13] O. Carrasco, R.B. Gomez, A. Chainani, W.E. Roper, Hyperspectral imaging applied to medical diagnoses and food safety, in: Proc. SPIE 5097, Geo-Spatial and Temporal Image and Data Exploitation III, 2003, pp. 215–221.
[14] M.A. Afromowitz, J.B. Callis, D.M. Heimbach, L.A. DeSoto, M.K. Norton, Multispectral imaging of burn wounds: a new clinical instrument for evaluating burn depth, IEEE Transactions on Biomedical Engineering 35 (10) (1988) 842–850.
[15] G. Zonios, et al., Diffuse reflectance spectroscopy of human adenomatous colon polyps in vivo, Applied Optics 38 (31) (1999) 6628–6637.
[16] L.V. Wang, H.-I. Wu, Introduction, in: Biomedical Optics, John Wiley & Sons, Inc., 2009, pp. 1–15.
[17] B. Costas, P. Christos, E. George, Multi/hyper-spectral imaging, in: Handbook of Biomedical Optics, CRC Press, 2011, pp. 131–164.
[18] V.V. Tuchin, V. Tuchin, Tissue Optics: Light Scattering Methods and Instruments for Medical Diagnosis, SPIE press Bellingham, 2007.
[19] D.G. Ferris, et al., Multimodal hyperspectral imaging for the noninvasive diagnosis of cervical neoplasia, Journal of Lower Genital Tract Disease 5 (2) (2001) 65–72.
[20] M.C. Pierce, et al., Accuracy of in vivo multimodal optical imaging for detection of oral neoplasia, Cancer Prevention Research 5 (6) (2012) 801–809.
[21] M. Joel, V.-D. Tuan, Optical properties of tissue, in: Biomedical Photonics Handbook, CRC Press, 2003.
[22] M. Patterson, B. Wilson, D. Wyman, The propagation of optical radiation in tissue I. Models of radiation transport and their application, Lasers in Medical Science vol. 6 (2) (1991) 155–168 (in English).
[23] Y. Zhang, Y. Chen, Y. Yu, X. Xue, V.V. Tuchin, D. Zhu, Visible and near-infrared spectroscopy for distinguishing malignant tumor tissue from benign tumor and normal breast tissues in vitro, Journal of Biomedical Optics 18 (7) (July 2013) 077003 (in English).
[24] A. Welch, M.C. Gemert, W. Star, Definitions and overview of tissue optics, in: A.J. Welch, M.J.C. Gemert (Eds.), Optical-Thermal Response of Laser-Irradiated Tissue, Springer Netherlands, 2011, pp. 27–64.
[25] A. Roggan, K. Dörschel, O. Minet, D. Wolff, G. Müller, The optical properties of biological tissue in the near infrared wavelength range: review and measurements, in: LITT: Laser-Induced Interstitial Thermotherapy, Workshop, 1995, pp. 10–44.
[26] J.A. Freeberg, J.L. Benedet, C. MacAulay, L.A. West, M. Follen, The performance of fluorescence and reflectance spectroscopy for the in vivo diagnosis of cervical neoplasia; point probe versus multispectral approaches, Gynecologic Oncology 107 (Suppl. 1) (2007) S248–S255.
[27] V.-D. Tuan, M.C. Brian, Fluorescence spectroscopy for biomedical diagnostics, in: Biomedical Photonics Handbook, CRC Press, 2003.
[28] V.T. Valery, Light-tissue interactions, in: Biomedical Photonics Handbook, CRC Press, 2003.
[29] M. Sasha, M. Jelena, F. Michael, Reflectance spectroscopy, in: Handbook of Biomedical Optics, CRC Press, 2011, pp. 103–130.
[30] D. Roblyer, et al., Multispectral optical imaging device for in vivo detection of oral neoplasia, Journal of Biomedical Optics 13 (2) (2008) 024019.
[31] K.R. Koh, T.C. Wood, R.D. Goldin, G.-Z. Yang, D.S. Elson, Visible and Near Infrared Autofluorescence and Hyperspectral Imaging Spectroscopy for the Investigation of Colorectal Lesions and Detection of Exogenous Fluorophores, 2009, p. 71691E.
[32] K.J. Zuzak, et al., Characterization of a near-infrared laparoscopic hyperspectral imaging system for minimally invasive surgery, Analytical Chemistry 79 (12) (2007) 4709–4715.

[33] J.M. Benavides, et al., Multispectral digital colposcopy for in vivo detection of cervical cancer, Optics Express 11 (10) (2003) 1223−1236.

[34] Y. Hirohara, et al., Validity of retinal oxygen saturation analysis: hyperspectral imaging in visible wavelength with fundus camera and liquid crystal wavelength tunable filter, Optical Review 14 (3) (2007) 151−158.

[35] A.A. Fawzi, N. Lee, J.H. Acton, A.F. Laine, R.T. Smith, Recovery of macular pigment spectrum in vivo using hyperspectral image analysis, Journal of Biomedical Optics 16 (10) (2011) 106008.

[36] X. Liu, D.A. Rice, B. Khoobehi, Spectral Reflectance of the Ocular Fundus as a Diagnostic Marker for Cerebral Malaria, 2012, p. 82290H.

[37] S. Begin, B. Burgoyne, V. Mercier, A. Villeneuve, R. Vallee, D. Cote, Coherent anti-stokes Raman scattering hyperspectral tissue imaging with a wavelength-swept system, Biomedical Optics Express 2 (5) (2011) 1296−1306 (in English).

[38] H. Tsurui, et al., Hyperspectral Imaging of Pathology Samples, 1999, pp. 273−281.

[39] S. Shah, et al., Cutaneous wound analysis using hyperspectral imaging, Biotechniques 34 (2) (2003) 408−413.

[40] B.S. Sorg, B.J. Moeller, O. Donovan, Y. Cao, M.W. Dewhirst, Hyperspectral imaging of hemoglobin saturation in tumor microvasculature and tumor hypoxia development, Journal of Biomedical Optics 10 (4) (2005) 44004.

[41] K. Masood, N. Rajpoot, K. Rajpoot, H. Qureshi, Hyperspectral colon tissue classification using morphological analysis, in: Emerging Technologies ICET '06. International Conference on, 2006, 2006, pp. 735−741.

[42] Q. Li, Y. Xue, G. Xiao, J. Zhang, Study on microscope hyperspectral medical imaging method for biomedical quantitative analysis, Chinese Science Bulletin 53 (9) (2008) 1431−1434.

[43] K. Masood, N. Rajpoot, Spatial analysis for colon biopsy classification from hyperspectral imagery, Annals of the BMVA 2008 (4) (2008) 1−16.

[44] L.L. Randeberg, E.L.P. Larsen, L.O. Svaasand, Hyperspectral imaging of blood perfusion and chromophore distribution in skin, 2009, pp. 71610C-71610C.

[45] G.M. Palmer, A.N. Fontanella, G. Zhang, G. Hanna, C.L. Fraser, M.W. Dewhirst, Optical imaging of tumor hypoxia dynamics, Journal of Biomedical Optics 15 (6) (2010) 066021.

[46] J. Schweizer, J. Hollmach, G. Steiner, L. Knels, R.H. Funk, E. Koch, Hyperspectral imaging - a new modality for eye diagnostics, Biomedizinische Technik (2012) (in English).

[47] U. Maeder, et al., Evaluation and quantification of spectral information in tissue by confocal microscopy, Journal of Biomedical Optics 17 (10) (2012), 106011−1.

[48] R.A. Schultz, T. Nielsen, J.R. Zavaleta, R. Ruch, R. Wyatt, H.R. Garner, Hyperspectral imaging: a novel approach for microscopic analysis, Cytometry 43 (4) (2001) 239−247.

[49] P. Constantinou, R.S. Dacosta, B.C. Wilson, Extending immunofluorescence detection limits in whole paraffin-embedded formalin fixed tissues using hyperspectral confocal fluorescence imaging, Journal of Microscopy 234 (2) (2009) 137−146 (in English).

[50] D. Landgrebe, Hyperspectral image data analysis, Signal Processing Magazine, IEEE 19 (1) (2002) 17−28.

[51] S.G. Kong, Z. Du, M. Martin, T. Vo-Dinh, Hyperspectral fluorescence image analysis for use in medical diagnostics, in: T. VoDinh, W.S. Grundfest, D.A. Benaron, G.E. Cohn (Eds.), Advanced Biomedical and Clinical Diagnostic Systems III, Proceedings of the Society of Photo-Optical Instrumentation Engineers (Spie), vol. 5692, Spie-Int Soc Optical Engineering, Bellingham, 2005, pp. 21−28.

[52] S.T. Monteiro, Y. Kosugi, K. Uto, E. Watanabe, Towards applying hyperspectral imagery as an intraoperative visual aid tool, Visualization Imaging and Image Processing (2004) 483−488.

[53] Z. Liu, H.J. Wang, Q.L. Li, Tongue tumor detection in medical hyperspectral images, Sensors 12 (1) (2012) 162−174 (in English).
[54] M.G. Sowa, J.R. Payette, M.D. Hewko, H.H. Mantsch, Visible-near infrared multispectral imaging of the rat dorsal skin flap, Journal of Biomedical Optics 4 (4) (1999) 474−481.
[55] R. Gillies, et al., Systemic effects of shock and resuscitation monitored by visible hyperspectral imaging, Diabetes Technology & Therapeutics 5 (5) (2003) 847−855.
[56] S.V. Panasyuk, et al., Medical hyperspectral imaging to facilitate residual tumor identification during surgery, Cancer Biology & Therapy 6 (3) (2007) 439−446 (in English).
[57] H. Lange, R. Baker, J. Håkansson, U. Gustafsson, S. a. T. International, Reflectance and fluorescence hyperspectral elastic image registration, Medical Imaging 5370 (2004) 335−2590.
[58] A. Plaza, et al., Recent advances in techniques for hyperspectral image processing, Remote Sensing of Environment 113 (Suppl. 1) (2009) S110−S122.
[59] M. Fauvel, Y. Tarabalka, J. n. A. Benediktsson, J. Chanussot, J.C. Tilton, Advances in spectral−spatial classification of hyperspectral images, Proceedings of the IEEE (2012).
[60] K.J. Zuzak, S.C. Naik, G. Alexandrakis, D. Hawkins, K. Behbehani, E. Livingston, Intraoperative bile duct visualization using near-infrared hyperspectral video imaging, The American Journal of Surgery 195 (4) (2008) 491−497.
[61] A.O.H. Gerstner, et al., Hyperspectral imaging of mucosal surfaces in patients, Journal of Biophotonics 5 (3) (2012) 255−262.
[62] P.A. Bautista, Y. Yagi, Digital simulation of staining in histopathology multispectral images: enhancement and linear transformation of spectral transmittance, Journal of Biomedical Optics 17 (5) (2012), 056013-1.
[63] E.L.P. Larsen, L.L. Randeberg, E. Olstad, O.A. Haugen, A. Aksnes, L.O. Svaasand, Hyperspectral imaging of atherosclerotic plaques in vitro, Journal of Biomedical Optics 16 (2) (2011) 026011.
[64] I. Guyon, A Elisseeff, "An introduction to variable and feature selection, Journal of Machine Learning Research 3 (2003) 1157−1182.
[65] D. Lu, Q. Weng, A survey of image classification methods and techniques for improving classification performance, International Journal of Remote Sensing 28 (5) (2007) 823−870.
[66] F. Melgani, L. Bruzzone, Classification of hyperspectral remote sensing images with support vector machines, IEEE Transactions on Geoscience and Remote Sensing 42 (8) (2004) 1778−1790.
[67] Z. Liu, J.Q. Yan, D. Zhang, Q.L. Li, Automated tongue segmentation in hyperspectral images for medicine, Applied Optics 46 (34) (2007) 8328−8334 (in English).
[68] Z. Liu, D. Zhang, J.Q. Yan, Q.L. Li, Q.L. Tang, Classification of hyperspectral medical tongue images for tongue diagnosis, Computerized Medical Imaging and Graphics 31 (8) (2007) 672−678 (in English).
[69] H. Akbari, et al., Hyperspectral imaging and quantitative analysis for prostate cancer detection, Journal of Biomedical Optics 17 (7) (2012) 076005 (in English).
[70] H. Akbari, L.V. Halig, H. Zhang, D. Wang, Z.G. Chen, B. Fei, Detection of cancer metastasis using a novel macroscopic hyperspectral method, Biomedical Applications in Molecular, Structural, and Functional Imaging 8317 (2012).
[71] H. Akbari, Y. Kosugi, K. Kojima, N. Tanaka, Blood vessel detection and artery-vein differentiation using hyperspectral imaging, in: Engineering in Medicine and Biology Society EMBC 2009. Annual International Conference of the IEEE, 2009, pp. 1461−1464.
[72] H. Akbari, K. Uto, Y. Kosugi, K. Kojima, N. Tanaka, Cancer detection using infrared hyperspectral imaging, Cancer Science 102 (4) (2011) 852−857.

[73] S. Kong, L.-J. Park, Hyperspectral image analysis for skin tumor detection, in: R. Hammoud (Ed.), Augmented Vision Perception in Infrared, Advances in Pattern Recognition, Springer London, 2009, pp. 155−171.

[74] K. Masood, N. Rajpoot, Texture based classification of hyperspectral colon biopsy samples using CLBP, in: ISBI '09. IEEE International Symposium on, 2009 Biomedical Imaging: From Nano to Macro, 2009, pp. 1011−1014.

[75] H. Akbari, Y. Kosugi, K. Kojima, N. Tanaka, Wavelet-based compression and segmentation of hyperspectral images in surgery, in: T. Dohi, I. Sakuma, H. Liao (Eds.), Medical Imaging and Augmented Reality, Lecture Notes in Computer Science, vol. 5128, Springer Berlin Heidelberg, 2008, pp. 142−149.

[76] R. Jolivot, P. Vabres, F. Marzani, Reconstruction of hyperspectral cutaneous data from an artificial neural network-based multispectral imaging system, Computerized Medical Imaging and Graphics 35 (2) (2011) 85−88.

[77] F. Blanco, M. López-Mesas, S. Serranti, G. Bonifazi, J. Havel, M. Valiente, Hyperspectral imaging based method for fast characterization of kidney stone types, Journal of Biomedical Optics 17 (7) (2012), 076027-1.

[78] K. Rajpoot, N. Rajpoot, SVM optimization for hyperspectral colon tissue cell classification, in: C. Barillot, D. Haynor, P. Hellier (Eds.), Medical Image Computing and Computer-Assisted Intervention − MICCAI 2004, Lecture Notes in Computer Science, vol. 3217, Springer Berlin Heidelberg, 2004, pp. 829−837.

[79] M. Fauvel, J.A. Benediktsson, J. Chanussot, J.R. Sveinsson, Spectral and spatial classification of hyperspectral data using SVMs and morphological profiles, IEEE Transactions on Geoscience and Remote Sensing 46 (11) (2008) 3804−3814.

[80] G. Hughes, On the mean accuracy of statistical pattern recognizers, IEEE Transactions on Information Theory 14 (1) (1968) 55−63.

[81] Y. Guan, Q. Li, Y. Wang, H. Liu, Z. Zhu, Pathological leucocyte segmentation algorithm based on hyperspectral imaging technique, Optical Engineering 51 (5) (2012), 053202-1.

[82] R. Martin, B. Thies, A. Gerstner, Hyperspectral hybrid method classification for detecting altered mucosa of the human larynx, International Journal of Health Geographics 11 (1) (2012) 21.

[83] L. Qingli, W. Yiting, L. Hongying, C. Zenggan, Nerve fibers identification based on molecular hyperspectral imaging technology, in: 2012 IEEE International Conference on Computer Science and Automation Engineering (CSAE) 3, 2012, pp. 15−17.

[84] N. Keshava, J.F. Mustard, Spectral unmixing, Signal Processing Magazine, IEEE 19 (1) (2002) 44−57.

[85] L.C. Parra, C. Spence, P. Sajda, A. Ziehe, K.-R. Müller, Unmixing hyperspectral data, News in Physiological Sciences (1999) 942−948.

[86] M. Berman, A. Phatak, R. Lagerstrom, B.R. Wood, ICE: a new method for the multivariate curve resolution of hyperspectral images, Journal of Chemometrics 23 (2) (2009) 101−116.

[87] G. Begelman, M. Zibulevsky, E. Rivlin, T. Kolatt, Blind decomposition of transmission light microscopic hyperspectral cube using sparse representation, IEEE Transactions on Medical Imaging 28 (8) (2009) 1317−1324.

[88] L.C. Cancio, et al., Hyperspectral imaging: a new approach to the diagnosis of hemorrhagic shock, The Journal of Trauma and Acute Care Surgery 60 (5) (2006) 1087−1095. https://doi.org/10.1097/01.ta.0000217357.10617.3d.

[89] L.C. Cancio, Application of novel hyperspectral imaging technologies in combat casualty care, Proceedings of the SPIE (2010) 759605.

[90] J.A. Chin, E.C. Wang, M.R. Kibbe, Evaluation of hyperspectral technology for assessing the presence and severity of peripheral artery disease, Journal of Vascular Surgery 54 (6) (2011) 1679−1688.
[91] P. Usenik, M. Bürmen, A. Fidler, F. Pernuš, B. Likar, Evaluation of Cross-Polarized Near Infrared Hyperspectral Imaging for Early Detection of Dental Caries, 2012, p. 82080G.
[92] S. S. A., et al., Cutaneous Wound Analysis Using Hyperspectral Imaging (No. 2), ETATS-UNIS: Eaton, Natick, MA, 2003, p. 5.
[93] K.R. Bambery, B.R. Wood, M.A. Quinn, D. McNaughton, Fourier transform infrared imaging and unsupervised hierarchical clustering applied to cervical biopsies, Australian Journal of Chemistry 57 (12) (2004) 1139−1143.
[94] R.L. Greenman, et al., Early changes in the skin microcirculation and muscle metabolism of the diabetic foot, The Lancet 366 (9498) (2005) 1711−1717.
[95] S.G. KONG, M.E. MARTIN, VO-DINH, Tuan, Hyperspectral Fluorescence Imaging for Mouse Skin Tumor Detection (No. 6), COREE, REPUBLIQUE DE: Electronics and Telecommunications Research Institute, Taejon, 2006, p. 7.
[96] D.T. Dicker, et al., Differentiation of normal skin and melanoma using high resolution hyperspectral imaging, Cancer Biology & Therapy 5 (8) (2006) 1033−1038.
[97] L.L. Randeberg, I. Baarstad, T. Løke, P. Kaspersen, L.O. Svaasand, Hyperspectral imaging of bruised skin, in: Proc. SPIE 6078, Photonic Therapeutics and Diagnostics II, 2006, p. 60780O.
[98] L.L. Randeberg, J. Hernandez-Palacios, Hyperspectral imaging of bruises in the SWIR spectral region, in: Proc. SPIE 8207, Photonic Therapeutics and Diagnostics VIII vol. 8207, 2012, pp. 82070N-82070N-10.
[99] W.R. Johnson, D.W. Wilson, W. Fink, M. Humayun, G. Bearman, Snapshot hyperspectral imaging in ophthalmology, Journal of Biomedical Optics, Research Support, Non-U.S. Gov't Research Support, U.S. Gov't, Non-P.H.S. 12 (1) (2007) 014036 (in English).
[100] H. Akbari, Y. Kosugi, K. Kojima, N. Tanaka, Detection and analysis of the intestinal ischemia using visible and invisible hyperspectral imaging, IEEE Transactions on Biomedical Engineering 57 (8) (2010) 2011−2017.
[101] R.T. Kester, N. Bedard, L. Gao, T.S. Tkaczyk, Real-time snapshot hyperspectral imaging endoscope, Journal of Biomedical Optics 16 (5) (2011) 056005 (in English).
[102] D. Yudovsky, A. Nouvong, K. Schomacker, L. Pilon, Assessing diabetic foot ulcer development risk with hyperspectral tissue oximetry, Journal of Biomedical Optics 16 (2) (2011) 026009.
[103] K. Mitra, et al., Indocyanine-green-loaded microballoons for biliary imaging in cholecystectomy, Journal of Biomedical Optics 17 (11) (2012) 116025.
[104] T.E. Renkoski, K.D. Hatch, U. Utzinger, Wide-field spectral imaging of human ovary autofluorescence and oncologic diagnosis via previously collected probe data, Journal of Biomedical Optics 17 (3) (2012), 036003-1.
[105] J.G. Rosas, M. Blanco, A criterion for assessing homogeneity distribution in hyperspectral images. Part 2: application of homogeneity indices to solid pharmaceutical dosage forms, Journal of Pharmaceutical and Biomedical Analysis 70 (0) (2012) 691−699.
[106] A.O.N. Joseph, Hyperspectral Optical Imaging for Detection, Diagnosis and Staging of Cancer, Thesis, 2012.
[107] L.V. Wang, H.-i. Wu, Biomedical Optics: Principles and Imaging, Wiley-Interscience, 2012.
[108] K. Sokolov, M. Follen, R. Richards-Kortum, Optical spectroscopy for detection of neoplasia, Current Opinion in Chemical Biology 6 (5) (2002) 651−658.

[109] A.M. Siddiqi, et al., Use of hyperspectral imaging to distinguish normal, precancerous, and cancerous cells, Cancer Cytopathology 114 (1) (2008) 13−21.

[110] I. Pavlova, K. Sokolov, R. Drezek, A. Malpica, M. Follen, R. Richards-Kortum, Microanatomical and biochemical origins of normal and precancerous cervical autofluorescence using laser-scanning fluorescence confocal microscopy, Photochemistry and Photobiology 77 (5) (2003) 550−555 (in English).

[111] L. Boucheron, Z. Bi, N. Harvey, B. Manjunath, D. Rimm, Utility of multispectral imaging for nuclear classification of routine clinical histopathology imagery, BMC Cell Biology 8 (Suppl. 1) (2007) S8.

[112] S. Argov, et al., Diagnostic potential of fourier-transform infrared microspectroscopy and advanced computational methods in colon cancer patients, Journal of Biomedical Optics 7 (2) (2002) 248−254.

[113] M. Maggioni, et al., Hyperspectral Microscopic Analysis of Normal, Benign and Carcinoma Microarray Tissue Sections, 2006, p. 60910I.

[114] K.M. Rajpoot, N.M. Rajpoot, Wavelet based segmentation of hyperspectral colon tissue imagery, in: Multi Topic Conference, 2003. INMIC 2003. 7th International, 2003, pp. 38−43.

[115] K. Rajpoot, N. Rajpoot, SVM optimization for hyperspectral colon tissue cell classification, in: Medical Image Computing and Computer-Assisted Intervention − MICCAI, vol. 3217, 2004, pp. 829−837.

[116] K. Masood, N.M. Rajpoot, Classification of colon biopsy samples by spatial analysis of a single spectral band from its hyperspectral cube, in: 11th Medical Image Understanding and Analysis (MIUA 2007), 2007. Conference or Workshopp. 17−18 July.

[117] K. Masood, Hyperspectral imaging with wavelet transform for classification of colon tissue biopsy samples, 2008, pp. 707319−707319.

[118] M. Hohmann, et al., Preliminary Results for Hyperspectral Videoendoscopy Diagnostics on the Phantoms of Normal and Abnormal Tissues: Towards Gastrointestinal Diagnostics, 2011, p. 80872N.

[119] S. Kiyotoki, et al., New method for detection of gastric cancer by hyperspectral imaging: a pilot study, Journal of Biomedical Optics 18 (2) (2013) 026010.

[120] D. Hattery, M. Hassan, S. Demos, A. Gandjbakhche, Hyperspectral imaging of Kaposi's Sarcoma for disease assessment and treatment monitoring, in: Applied Imagery Pattern Recognition Workshop, 2002. Proceedings. 31st, 2002, pp. 124−130.

[121] C. Angeletti, N.R. Harvey, V. Khomitch, A.H. Fischer, R.M. Levenson, D.L. Rimm, Detection of malignancy in cytology specimens using spectral−spatial analysis, Laboratory Investigation 85 (12) (2005) 1555−1564.

[122] M.E. Martin, M.B. Wabuyele, M. Panjehpour, M.N. Phan, B.F. Overholt, T. Vo-Dinh, Hyperspectral fluorescence imaging system for biomedical diagnostics, in: Proc. SPIE 6080, Advanced Biomedical and Clinical Diagnostic Systems IV, 2006, p. 60800Q.

[123] M.E. Martin, et al., Development of an Advanced Hyperspectral Imaging (HSI) system with application for cancer detection, Annals of Biomedical Engineering 34 (6) (2006) 1061−1068.

[124] D. Roblyer, C. Kurachi, A.M. Gillenwater, R. Richards-Kortum, In vivo fluorescence hyperspectral imaging of oral neoplasia, Proceedings of the SPIE (2009), 71690J-71690J-10.

[125] D. Roblyer, et al., Objective detection and delineation of oral neoplasia using autofluorescence imaging, Cancer Prevention Research 2 (5) (2009) 423−431.

[126] M. Isabelle, K. Rogers, N. Stone, Correlation mapping: rapid method for identification of histological features and pathological classification in mid infrared spectroscopic images of lymph nodes, Journal of Biomedical Optics 15 (2) (2010), 026030-026030-5.

[127] A.J. Chaudhari, et al., Hyperspectral and multispectral bioluminescence optical tomography for small animal imaging, Physics in Medicine and Biology 50 (23) (2005) 5421−5441 (in English).
[128] J.W. Uhr, et al., Molecular profiling of individual tumor cells by hyperspectral microscopic imaging, Translational Research 159 (5) (2012) 366−375.
[129] L.G. Koss, The papanicolaou test for cervical cancer detection. A triumph and a tragedy, Journal of the American Medical Association 261 (5) (1989) 737−743 (in English).
[130] N. Ramanujam, Fluorescence spectroscopy of neoplastic and non-neoplastic tissues, Neoplasia 2 (1−2) (2000) 89−117 (in English).
[131] B.R. Wood, L. Chiriboga, H. Yee, M.A. Quinn, D. McNaughton, M. Diem, Fourier transform infrared (FTIR) spectral mapping of the cervical transformation zone, and dysplastic squamous epithelium, Gynecologic Oncology 93 (1) (2004) 59−68.
[132] R. Siegel, D. Naishadham, A. Jemal, Cancer statistics, 2012, CA: A Cancer Journal for Clinicians 62 (1) (2012) 10−29.
[133] S.M. Ismail, et al., Observer variation in histopathological diagnosis and grading of cervical intraepithelial neoplasia, BMJ British Medical Journal 298 (6675) (1989) 707.
[134] C. Weber, H. Noels, Atherosclerosis: current pathogenesis and therapeutic options, Nature Medicine 17 (11) (2011) 1410−1422.
[135] C. Kittrell, et al., Diagnosis of fibrous arterial atherosclerosis using fluorescence, Applied Optics 24 (15) (1985) 2280−2281.
[136] S. Andersson-Engels, J. Johansson, U. Stenram, K. Svanberg, S. Svanberg, Malignant tumor and atherosclerotic plaque diagnosis using laser-induced fluorescence, IEEE Journal of Quantum Electronics 26 (12) (1990) 2207−2217.
[137] G.O. Angheloiu, et al., Intrinsic fluorescence and diffuse reflectance spectroscopy identify superficial foam cells in coronary plaques prone to erosion, Arteriosclerosis, Thrombosis, and Vascular Biology 26 (7) (2006) 1594−1600.
[138] W.R. Hiatt, M.R. Nehler, Peripheral Arterial Disease, 2007.
[139] K.J. Zuzak, M.T. Gladwin, R.O. Cannon, I.W. Levin, Imaging hemoglobin oxygen saturation in sickle cell disease patients using noninvasive visible reflectance hyperspectral techniques: effects of nitric oxide, American Journal of Physiology - Heart and Circulatory Physiology 285 (3) (2003) H1183−H1189.
[140] R. Neville, S. Gupta, Establishment of normative perfusion values using hyperspectral tissue oxygenation mapping technology, Vascular Disease Management 6 (6) (2009).
[141] D. Cohen, M. Arnoldussen, G. Bearman, W.S. Grundfest, The use of spectral imaging for the diagnosis of retinal disease, in: LEOS '99. IEEE Lasers and Electro-Optics Society 1999 12th Annual Meeting vol. 1, 1999, pp. 220−221.
[142] B. Khoobehi, J.M. Beach, H. Kawano, Hyperspectral imaging for measurement of oxygen saturation in the optic nerve head, Investigative Ophthalmology & Visual Science 45 (5) (2004) 1464−1472.
[143] L.K. Cheung, A. Eaton, Age-related macular degeneration, Pharmacotherapy: The Journal of Human Pharmacology and Drug Therapy (2013).
[144] D.G. Armstrong, B.A. Lipsky, N. Singh, Preventing foot ulcers in patients with diabetes, Journal of the American Medical Association 293 (2) (2005) 217−228.
[145] L. Khaodhiar, et al., The use of medical hyperspectral technology to evaluate microcirculatory changes in diabetic foot ulcers and predict clinical outcomes, Diabetes Care (2007).
[146] D. Yudovsky, A. Nouvong, L. Pilon, Hyperspectral imaging in diabetic foot wound care, Journal of Diabetes Science and Technology 4 (5) (2010) 1099−1113.

[147] D. Yudovsky, A. Nouvong, K. Schomacker, L. Pilon, Monitoring temporal development and healing of diabetic foot ulceration using hyperspectral imaging, Journal of Biophotonics 4 (7−8) (2011) 565−576 (in English).

[148] K.J. Zuzak, et al., Visible and infrared hyperspectral visualization of normal and ischemic tissue, in: [Engineering in Medicine and Biology, 1999. 21st Annual Conf. and the 1999 Annual Fall Meeting of the Biomedical Engineering Soc.] BMES/EMBS Conference, 1999. Proceedings of the First Joint, vol. 2, 1999, p. 1118.

[149] K.J. Zuzak, M.D. Schaeberle, E.N. Lewis, I.W. Levin, Visible spectroscopic imaging studies of normal and ischemic dermal tissue, 2000, pp. 17−26.

[150] K.J. Zuzak, M.D. Schaeberle, M.T. Gladwin, R.O. Cannon, I.W. Levin, Noninvasive determination of spatially resolved and time-resolved tissue perfusion in humans during nitric oxide inhibition and inhalation by use of a visible-reflectance hyperspectral imaging technique, Circulation 104 (24) (2001) 2905−2910.

[151] K.J. Zuzak, M.D. Schaeberle, E.N. Lewis, I.W. Levin, Visible reflectance hyperspectral imaging: characterization of a noninvasive, in vivo system for determining tissue perfusion, Analytical Chemistry 74 (9) (2002) 2021−2028.

[152] M.L. Huebschman, K.P. Rosenblatt, H.R. Garner, Hyperspectral microscopy imaging to analyze pathology samples with multicolors reduces time and cost, in: Proc. SPIE 7182, Imaging, Manipulation, and Analysis of Biomolecules, Cells, and Tissues VII, 2009, p. 71821F.

[153] F. Vasefi, et al., Transillumination hyperspectral imaging for histopathological examination of excised tissue, Journal of Biomedical Optics 16 (8) (2011) 086014.

[154] B. Khoobehi, A. Khoobehi, P. Fournier, Snapshot hyperspectral imaging to measure oxygen saturation in the retina using fiber bundle and multi-slit spectrometer, in: Proc. SPIE 8229, Optical Diagnostics and Sensing XII: Toward Point-of-Care Diagnostics; and Design and Performance Validation of Phantoms Used in Conjunction with Optical Measurement of Tissue IV, 2012, p. 82291E.

[155] J. Freeman, et al., Multispectral and hyperspectral imaging: applications for medical and surgical diagnostics, in: Proceedings of the 19th Annual International Conference of the Ieee Engineering in Medicine and Biology Society, Vol 19, Pts 1-6: Magnificent Milestones and Emerging Opportunities in Medical Engineering, Vol. 19(Proceedings of Annual International Conference of the Ieee Engineering in Medicine and Biology Society, IEEE, New York, 1997, pp. 700−701.

[156] S.T. Monteiro, K. Uto, Y. Kosugi, E. Watanabe, Towards a surgical tool using hyperspectral imagery as visual aid, in: Proc. MICCAI AMI-ARCS 2004, 2004, pp. 97−103.

[157] K.J. Zuzak, R.P. Francis, E.F. Wehner, M. Litorja, J.A. Cadeddu, E.H. Livingston, Active DLP hyperspectral illumination: a noninvasive, in vivo, system characterization visualizing tissue oxygenation at near video rates, Analytical Chemistry 83 (19) (2011) 7424−7430 (in English).

[158] E. Wehner, A. Thapa, E. Livingston, K. Zuzak, NIR DLPÃ Â® hyperspectral imaging system for medical applications, in: Proc. SPIE 7932, Emerging Digital Micromirror Device Based Systems and Applications III, 2011, pp. 793204−793204-9.

[159] M.S. Holzer, et al., Assessment of renal oxygenation during partial nephrectomy using hyperspectral imaging, The Journal of Urology 186 (2) (2011) 400−404.

[160] E.O. Olweny, et al., Renal oxygenation during robotic-assisted laparoscopic partial nephrectomy; characterization using laparoscopic digital light processing (DLP(R)) hyperspectral imaging, Journal of Endourology (2012) (in English).

[161] K.J. Zuzak, et al., Hyperspectral imaging utilizing LCTF and DLP technology for surgical and clinical applications, in: Proc. SPIE 7170, Design and Quality for Biomedical Technologies II, vol. 7170, 2009, p. 71700C.

[162] K.J. Zuzak, et al., DLP hyperspectral imaging for surgical and clinical utility, in: Proc. SPIE 7210, Emerging Digital Micromirror Device Based Systems and Applications, vol. 7210, 2009, p. 721006.
[163] K.J. Zuzak, et al., The robustness of DLP hyperspectral imaging for clinical and surgical utility, in: SPIE Proceedings: Biochemical Visualization for Clinical Applications, vol. 7596, 2010, p. 759604.
[164] H. Akbari, Y. Kosugi, K. Kojima, N. Tanaka, Hyperspectral imaging and diagnosis of intestinal ischemia, in: Engineering in Medicine and Biology Society, 2008. EMBS 2008. 30th Annual International Conference of the IEEE, 2008, pp. 1238–1241.
[165] B. Fisher, et al., Twenty-year follow-up of a randomized trial comparing total mastectomy, lumpectomy, and lumpectomy plus irradiation for the treatment of invasive breast cancer, New England Journal of Medicine 347 (16) (2002) 1233–1241 (in English).
[166] S.C. Campbell, et al., Guideline for management of the clinical T1 renal mass, The Journal of Urology 182 (4) (2009) 1271.
[167] B.A. Laven, et al., A pilot study of ice-slurry application for inducing laparoscopic renal hypothermia, BJU International 99 (1) (2007) 166–170.
[168] C.R. Tracy, et al., Characterization of renal ischemia using DLP hyperspectral imaging: a pilot study comparing artery-only occlusion versus artery and vein occlusion, Journal of Endourology 24 (3) (2010) 321–325 (in English).
[169] V.-D. Tuan, A hyperspectral imaging system for in vivo optical diagnostics, IEEE Engineering in Medicine and Biology Magazine 23 (5) (2004) 40–49.
[170] P. Zhihong, G. Healey, M. Prasad, B. Tromberg, Face recognition in hyperspectral images, IEEE Transactions on Pattern Analysis and Machine Intelligence 25 (12) (2003) 1552–1560.
[171] A. Kienle, L. Lilge, M.S. Patterson, R. Hibst, R. Steiner, B.C. Wilson, Spatially resolved absolute diffuse reflectance measurements for noninvasive determination of the optical scattering and absorption coefficients of biological tissue, Applied Optics 35 (13) (1996) 2304–2314.
[172] I. Georgakoudi, et al., Fluorescence, reflectance, and light-scattering spectroscopy for evaluating dysplasia in patients with Barrett's esophagus, Gastroenterology 120 (7) (2001) 1620–1629.
[173] I.J. Bigio, J.R. Mourant, Ultraviolet and visible spectroscopies for tissue diagnostics: fluorescence spectroscopy and elastic-scattering spectroscopy, Physics in Medicine and Biology 42 (5) (1997) 803.
[174] R. Doornbos, R. Lang, M. Aalders, F. Cross, H. Sterenborg, The determination of in vivo human tissue optical properties and absolute chromophore concentrations using spatially resolved steady-state diffuse reflectance spectroscopy, Physics in Medicine and Biology 44 (4) (1999) 967.
[175] M.G. Müller, et al., Spectroscopic detection and evaluation of morphologic and biochemical changes in early human oral carcinoma, Cancer 97 (7) (2003) 1681–1692.
[176] Y. Chung-Chieh, et al., Quantitative spectroscopic imaging for non-invasive early cancer detection, Optical Society of America 16 (20) (2008) 16227–16239.
[177] M.E. Martin, et al., An AOTF-based dual-modality hyperspectral imaging system (DMHSI) capable of simultaneous fluorescence and reflectance imaging, Medical Engineering & Physics 28 (2) (2005) 149–155.
[178] M. Patterson, B. Wilson, D. Wyman, The propagation of optical radiation in tissue. II: optical properties of tissues and resulting fluence distributions, Lasers in Medical Science 6 (4) (1991) 379–390 (in English).

[179] A. Kim, B. Wilson, Measurement of ex vivo and in vivo tissue optical properties: methods and theories, in: A.J. Welch, M.J.C. Gemert (Eds.), Optical-Thermal Response of Laser-Irradiated Tissue, Springer Netherlands, 2011, pp. 267−319.

[180] A.L. Vahrmeijer, M. Hutteman, J.R. van der Vorst, C.J. van de Velde, J.V. Frangioni, Image-guided cancer surgery using near-infrared fluorescence, Nature Reviews Clinical Oncology 10 (9) (2013) 507−518.